Abstract

The influence of particle shape of coating pigments on their packing ability and on the flow properties of coating colours has been investigated. The particle shapes considered were spherical, flaky and acicular (needle-shaped). In the case of suspensions containing monodisperse spherical polystyrene particles, a concentration gradient appeared in the filter cake forming during filtration under static conditions. Such a gradient, monitored by non-destructive magnetic resonance imaging (MRI), is not accounted for in the traditional filtration theory used in coating technology. Good agreement was found between a literature model describing filtration through a compressible filter cake and the concentration gradients measured by MRI. According to this model, the scaled concentration gradient was the same at all times.

For flaky (mainly kaolin) and acicular (aragonite) particles, a rapid method was evaluated to estimate a shape factor of the pigment particle. Generalised mathematical models of oblate and prolate spheroids were applied to reduce the three geometrical dimensions of the particle to two, the major axis and the minor axis. The shape factor, which is mass-based, was derived from a comparison between the results obtained by two different size-assessment instruments, viz. the Sedigraph and an instrument using light scattering. This yields a shape factor distribution as a function of equivalent spherical particle size, but the results are uncertain for small particle diameters, below 0.2 µm. Good agreement was obtained between the shape factor and a mass-based aspect ratio obtained by image analysis, but the rapid method is generally more accurate for flaky than for acicular particles.

Results obtained by capillary viscometry showed that there was a relationship between the viscosity at high shear rates ($>10^5$ s^{-1}) and the shape factor, but that it was not sufficient to use the median value of the shape factor to achieve proper information. A more complete evaluation requires knowledge of the shape factor distribution, which is also given in part by the method mentioned above. However, a large median shape factor was related to a high high-shear viscosity. Non-Newtonian entrance pressure losses were sometimes significant in capillary viscometry, indicating that it was inappropriate to measure the shear viscosity with only one capillary. Such effects were however relatively much more pronounced in slit die viscometry, especially in the case of acicular particles, where the aspect ratio was a crucial parameter. The influence of the shape factor of kaolin particles on the non-Newtonian entrance pressure losses over a slit die was surprisingly small. The high-shear viscosity of coating suspensions based on different pigments correlated with the median pore size of the corresponding coating layer rather than with the porosity.

Keywords: Aspect ratio, capillary viscometry, coating colour, filtration, particle packing, pigment, pore structure, rheology, shape factor, slit die viscometry, spheroid.

Scope of the thesis

The thesis includes the following papers, referred to by Roman numerals:

I. Lohmander, S, Martinez, M, Li, T-Q, Lason L and Rigdahl, M (1999)
Dewatering of coating dispersions – model experiments and analysis
Proc. Tappi Advanced Coating Fundam. Symp., Tappi Press, Atlanta, USA, 43
Accepted for publication in J. Pulp Paper Sci.

II. Lohmander, S (2000)
Aspect ratios of pigment particles determined by different methods
Nordic Pulp Pap. Res. J., **15**(3), 221

III. Lohmander, S and Rigdahl, M (2000)
Influence of a shape factor of pigment particles on the rheological properties of coating colours
Nordic Pulp Pap. Res. J., **15**(3), 231

IV. Lohmander, S
Influence of shape and a shape factor of pigment particles on the packing ability in coating layers
Accepted for publication in Nordic Pulp Pap. Res. J.

V. Lohmander, S and To, A
Rheological characterisation of coating colours – comparison between conventional techniques and a slit die system
Accepted for publication in Nordic Pulp Pap. Res. J.

VI. Dahlvik, P, Lohmander, S, Lason, L and Rigdahl, M (2000)
Relations between the rheological properties of coating colours and their performance in pilot-scale coating
Nordic Pulp Pap. Res. J., **15**(2), 106

Contents

1. Introduction

Paper and board materials are coated in order to improve their surfaces and the subsequent printing performance. Amongst the most important properties of the coated paper are a smooth surface, a high opacity and high brightness, sufficient mechanical strength to withstand the stresses during printing and a pore structure that interacts beneficially with the printing ink. The main constituent of the coating colour (the water-based suspension applied to the paper surface) is the pigment, usually kaolin clay and/or calcium carbonate, which is dispersed in water at a high solids content. Further, a latex binder (such as a styrene-butadiene copolymer) and a co-binder (such as starch or carboxymethyl cellulose, CMC) are added in order to ensure the required mechanical strength of the coating layer and to control the water retention of the coating colour during the coating process. Other components, such as optical brightners, preservatives and lubricating agents may also be included in the colour.

During blade coating, the coating colour is often applied to the paper surface by a roll, always in excess, and the surplus is scraped off by a blade, which evens and meters the coating colour so that a smooth surface is obtained. The interaction of the colour with the base paper leads to a penetration of the liquid phase into the porous structure of the coating base and an immobilisation of the coating layer. This penetration increases the solids content of the coating colour and, consequently, affects its rheological behaviour. The coating layer is further immobilised during the subsequent drying procedure, leading to a shrinkage of the structure. Even though rheology has been the subject of many investigations, coating colours as a multi-component phase seem to be a rather special group of fluids. High solids contents and machine speeds of up to 2000 m/min on industrial coaters and even higher on pilot plants are the origins of their special behaviour. With respect to coating runnability, the dewatering behaviour and the rheological properties of the colour are very crucial parameters.

A main factor affecting the water retention ability, rheological properties, runnability and final properties of coatings, is the packing ability of the pigment particles. This property is in turn affected by, e.g., particle size, size distribution, particle shape, shape distribution, and various colloidal forces including interactions with other components in the coating colour. Most pigment particles for the coating of paper and board are either flaky, like kaolin and talc, or more or less ”round”, like ground calcium carbonate (GCC), silica, polystyrene, and some grades of precipitated calcium carbonate (PCC). However, other shapes also exist, and amongst the most interesting is the needle-shaped (acicular) aragonite (PCC), which often has a complicated flow behaviour but sometimes yields a high quality coated paper (Engström, Rigdahl 1992).

The particle shapes considered in this work are flaky, acicular and (perfectly) spherical. A focus has been on kaolin, as this is the most commonly applied pigment world-wide together with GCC. Many properties of the pigment affect the coating operation, and amongst the most important are the particle shape and the aspect ratio, defined as the ratio of the diameter across the face of the particle to the thickness for flaky particles and as the ratio of the length to the diameter for acicular particles. The aspect ratio has traditionally been evaluated by means of Transmission Electron Microscopy (TEM), using a shadowing technique (Morris et al. 1965), but this method is time-consuming and subjective, and more objective, rapid and simple methods are required. This work evaluates the method for the determination of a shape factor developed by Jennings and Parslow (1988), which is based on a comparison between the results obtained from two different size-determining instruments, viz. the Sedigraph and an

instrument using light scattering. Generalised mathematical models of oblate and prolate spheroids were applied in order to reduce the three geometrical dimensions of the particle to two, the major axis and the minor axis. This method yields a shape factor distribution as a function of equivalent spherical particle size, but the results are uncertain for small particle diameters (< 0.2 µm). The shape factor, which is mass-based, can be a valuable tool for comparison purposes, with regard to the rheological properties of the coating colour and the final properties of the coating layer, and this interesting area has consequently been examined as well.

Rheological properties of coating colours at high shear rates have received considerable attention in this work. An appropriate way of estimating the shear viscosity at high shear rates, > 100,000 s^{-1}, is to use capillary viscometry and capillaries of different dimensions (Willenbacher, Hanciogullari 1997). This makes it possible to apply those experimental corrections that are sometimes needed, i.e., corrections for non-Newtonian entrance pressure losses (EPL) (mainly due to elasticity and/or additional elongational viscosity effects apart from those of a Newtonian fluid) and wall slip (Willenbacher, Hanciogullari 1997; Greenblatt, Wilson 1995). If the viscosity curves obtained with capillaries of different dimensions coincide, the shear viscosity is properly measured by each capillary, and no experimental corrections for non-Newtonian EPL or wall slip are needed.

Capillary viscometry will often fail as a tool to predict runnability, since the conditions during blade coating are very complicated and the course of events is hardly predictable from a simple shear viscosity measurement. A further step to approach the geometry in the vicinity of the blade tip is to use a slit die in place of a capillary for rheological evaluation at high shear rates. The slit die has a rectangular geometry, with a gap size more similar to the distance between blade and paper during blade coating and a shearing distance similar to the thickness of the blade. The slit die rheometer for paper coatings was introduced a decade ago (Tsuji et al. 1990), but very few results seem to have been reported since then. In terms of predictability, it should be borne in mind that there are still many limitations, e.g., about 90 % of the colour is recirculated at all times in the real coating process. Nevertheless, interesting features appear using the slit die, especially a pronounced impact of non-Newtonian effects which it is difficult to study using only capillaries. Such effects may have a dramatic influence on the flow behaviour of coating colours, as shown by previous modellings and experiments using model solutions (Sullivan, Middleman 1986; Ohlsson, Isaksson 1995), as well as on the final properties of the coating.

It should be emphasised that this thesis is not largely concerned with chemical interactions in coating colours. This is of course a limitation, as clays of different origins may behave differently, and since chemical interactions in systems based on clay and calcium carbonate are very different. In some cases, it is also clear that the results obtained cannot be explained in terms of particle size and shape alone. However, no blends of pigments have been used in this work, and this excludes the possibility of interactions between different pigments. Also, the results obtained show in many cases that similar trends are obtained in the flow behaviour as in other properties depending on the packing ability of pigment particles, and this justifies the chosen approach.

Four main areas are treated in this thesis:

1) The packing of spherical particles during dewatering under static conditions
2) The evaluation of aspect ratios (shape factors) of pigment particles through
a) a rapid method based on a comparison between the results obtained by two different size-determining instruments (Jennings, Parslow 1988; Slepetys, Cleland 1993) and
b) shear viscosity measurements at different solids contents, from which another shape factor, the intrinsic viscosity, can be derived using the Dougherty-Krieger relationship (Krieger, Dougherty 1959; Krieger 1972)
3) The influence of the shape factor evaluated in 2a) on the shear viscosity at high shear rates ($>10^5$ s^{-1}) and on the entrance pressure losses, using capillary and slit die viscometry, as well as on the runnability during pilot-plant trials
4) The influence of the shape factor evaluated in 2a) on the pore structure of a coating layer, and on properties depending on the pore structure

The results obtained show that a concentration gradient appeared in the filter cake forming during filtration under static conditions when suspensions containing a model pigment (polystyrene spheres) were used. Such a gradient is not accounted for in traditional coating technology (Letzelter 1997). The shape factor evaluated by the rapid method correlated well with the aspect ratio determined by image analysis, when the latter values were transferred to mass-based values. However, the evaluation of the shape factor is an engineering approach which should be used to rank the samples rather than as absolute values. The shape factor, and the shape factor distribution as a function of equivalent spherical particle size, were found to be important parameters determining the rheological properties of coating colours at high shear rates, as well as the properties of coating layers. For instance, the median shape factor correlated with a high high-shear viscosity.

The porosity of a coating layer based on a fine kaolin clay with a low shape factor was in general higher than that of a coating based on a coarse clay with a high shape factor, but the average pore size was considerably larger for the coarser pigment. The trend in high shear viscosity of coating suspensions based on different pigments followed the trend in median pore size of the corresponding coating layer, rather than the trend in porosity. Pilot plant trials showed that runnability problems, such as streaks and stalagmite formation, occurred particularly in the case of coating colours based on delaminated clay with a high shape factor, rather than with English clay with a moderate shape factor. This was also in part due to the lower water retention ability of the former colours.

2. Theory

2.1 Filtration theory

For flow through fixed incompressible beds, the Darcy equation is applicable in most cases:

$$\frac{dP_l}{dz} = \frac{\eta\omega(1-\phi)}{k(\phi)} \qquad [1]$$

where P_l is the hydrostatic pressure used to force the liquid through the bed, η is the shear viscosity, ω the velocity of the fluid, ϕ the solidity (volume of particles/total volume), z the direction of flow and $k(\phi)$ the permeability function.

During dewatering of a suspension containing small particles (< 10 µm) separated by colloidal forces, however, the cake is gradually built up in time and cannot be assumed to be incompressible (Tiller et al. 1987). Consider a cylinder containing the suspension, subjected to a constant applied pressure P at one face and where only the liquid phase is allowed to pass through a filter at the other. The equations required to describe the dynamics are a mass balance, a force balance and Eq. [1] (Landman et al. 1991), assuming that inertia terms and shear forces in the bulk of the fluid and those exerted by the cylinder walls are negligible. A one-dimensional analysis is subsequently performed (Landman et al. 1991), so that the only variables are z and the time t.

If υ is the velocity of the particles, a mass balance yields:

$$\frac{\partial}{\partial t}(\phi) - \frac{\partial}{\partial z}(\phi\upsilon) = 0 \quad \text{(particles)} \qquad [2]$$

$$\frac{\partial}{\partial t}(1-\phi) - \frac{\partial}{\partial z}((1-\phi)\upsilon) = 0 \quad \text{(fluid)} \qquad [3]$$

Eqs. [2] and [3] yield:

$$\frac{\partial}{\partial z}[\phi\upsilon + (1-\phi)\omega] = 0 \qquad [4]$$

Integration of Eq. [4] with respect to z gives:

$$\phi\upsilon + (1-\phi)\omega = C_1(t) \qquad [5]$$

where $C_1(t)$ is a function of time. At the top of the suspension, the fluid and the particles move at the same velocity:

$$-\upsilon = -\omega = \frac{d}{dt}h(t) \qquad [6]$$

where $h(t)$ is the height of the suspension. Hence, Eqs. [5] and [6] yield:

$$\phi(-\frac{d}{dt}h(t)) + (1-\phi)(-\frac{d}{dt}h(t)) = C_1(t) \Rightarrow C_1(t) = -\frac{d}{dt}h(t) = \phi\upsilon + (1-\phi)\omega \quad [7]$$

The fluid velocity ω can be eliminated from Eq. [1] by substitution with Eq. [6]:

$$\frac{dP_l}{dz} = \frac{\eta(\omega-\upsilon)(1-\phi)}{k(\phi)} = \frac{\eta}{k(\phi)}[-\frac{dh}{dt} - \phi\upsilon - \upsilon + \phi\upsilon] = -\frac{\eta}{k(\phi)}[\upsilon + \frac{dh}{dt}] \qquad [8]$$

When a particle is trapped at the top of the cake, the friction due to the flow of the surrounding fluid tends to move the particle further downwards into the cake. The stress is transmitted from particle to particle in a complicated way and a compressive force P_s is created, which increases with decreasing distance from the filter. A force balance yields:

$$\frac{\partial P_s}{\partial z} = \frac{\partial P_l}{\partial z} \qquad [9]$$

Integration with respect to z gives

$$P_s + P_f = P \qquad [10]$$

P_s is a function of the solidity $\phi(z,t)$ and the relationship is often represented as a power-law function:

$$P_s(\phi) = f(\phi) = m\phi^n \qquad [11]$$

where m and n are constants. Further,

$$\frac{\partial P_s}{\partial z} = \frac{\partial P_s \partial \phi}{\partial \phi \partial z} = f'(\phi)\frac{\partial \phi}{\partial z} \qquad [12]$$

Substitution of Eq. [12] into [9] and then into [8] yields

$$\frac{\partial P_l}{\partial z} = -f'(\phi)\frac{\partial \phi}{\partial z} = -\frac{\eta(\upsilon + \frac{dh}{dt})}{k(\phi)} \qquad [13]$$

Rearrangement of Eq. [13] and multiplication by $\frac{\phi}{\phi}$ gives

$$\frac{\partial \phi}{\partial z} = \frac{\eta\phi(\upsilon + \frac{dh}{dt})}{k(\phi)f'(\phi)\phi} \Rightarrow \upsilon = \frac{\partial \phi}{\partial z}\frac{k(\phi)f(\phi)}{\eta\phi} - \frac{dh}{dt} \qquad [14]$$

Substitution of Eq. [14] into Eq. [2] yields:

$$\frac{\partial \phi}{\partial t} = \frac{\partial}{\partial z}\left[\frac{k(\phi) f(\phi)}{\eta}\frac{\partial \phi}{\partial z}\right] - \frac{dh}{dt}\frac{\partial \phi}{\partial z} \qquad [15]$$

The corresponding boundary and auxiliary conditions for Eq. [15] are

$$\phi(z,0) = \phi_o \qquad [16]$$

$$f(\phi(0,t)) = \Delta P \qquad [17]$$

$$\phi(\varphi(t),t) = \phi_o \qquad [18]$$

$$\left.\frac{\partial \phi}{\partial z}\right|_{z=0} = \frac{\eta}{k(\phi) f'(\phi)\phi}\frac{dh(t)}{dt} \qquad [19]$$

$$\left.\frac{\partial \phi}{\partial z}\right|_{z=\varphi(t)} = 0 \qquad [20]$$

where $\varphi(t)$ is the height of the cake and ϕ_0 is the original solidity of the suspension.

Condition [16] states that the initial solidity is uniform throughout the vessel; [17] states that the compressive pressure at the bottom of the filter cake is equal to the applied pressure at all times; [18] states that the solidity at the top of the cake is equal to the initial solidity in the dispersion at all times; and [19] and [20] result from the fact that the velocity of the particles is zero at the filter and is equal to the velocity of the liquid phase at the top of the cake.

A mass balance over the cylinder yields

$$\phi_o H_o = \phi_o\left(h(t) - \varphi(t)\right) + \int_o^{\varphi(t)} \phi(z,t)\,dz \qquad [21]$$

where H_0 is the original height of the suspension. Landman et al. (1991) solved Eqs. [15]-[21] numerically through a scaling procedure and a Runge-Kutta shooting iteration process, but they can also be solved using the analytical method outlined in paper I. Such an analysis gives at hand that the volume of filtrate $V(t)$ can be expressed as

$$V(t) = A_F\sqrt{2\alpha\frac{\hat{\phi}(t) - \phi_o}{\phi_o}\frac{k(\phi(0,t))\Delta P}{\eta}t} \qquad [22]$$

where A_F is the filtration area, $\hat{\phi}(t)$ is the average solidity of the filter cake and α is a constant between 0 and 1 which can be shown to be related to the concentration gradient of the filter cake at $z = 0$; and $k(\phi(0,t))$ is the permeability evaluated at the surface of the filter.

This analysis has shown that the volume of filtrate from a given experiment in the compressible case can be written in virtually the same way as in the traditional incompressible case (Coulson, Richardson 1978), except that the constant α is included in the former case and the permeability of the cake is evaluated nearest the filter.

2.2 Spheres and spheroids

In this section, the concept of a spheroid is defined and the surface area and the major dimension of such a body are compared to one another and to that of a sphere at a given volume.

The equation for a circle of diameter d is:

$$x^2 + y^2 = \frac{d}{4}^2 \Rightarrow y = \sqrt{\frac{d}{4}^2 - x^2} \qquad [23]$$

The equation for an ellipse with the major axis a along the x-axis and the minor axis b along the y-axis is:

$$\frac{x^2}{a^2} + \frac{y^2}{b^2} = 1 \Rightarrow y = b\sqrt{1 - \frac{x^2}{a^2}} \qquad [24a]$$

$$\frac{x^2}{a^2} + \frac{y^2}{b^2} = 1 \Rightarrow x = a\sqrt{1 - \frac{y^2}{b^2}} \qquad [24b]$$

We define:

$$V = 2\pi \int f^2(x)dx \qquad [25a]$$

$$V = 2\pi \int f^2(y)dy \qquad [25b]$$

where V is the volume of a rotational body. The volume of a sphere V_s is obtained from Eqs. [23] and [25a]:

$$V_s = \frac{\pi}{6} d^3 \qquad [26]$$

The volume of an oblate spheroid V_{os} is obtained by letting the ellipse in Eq. [24] rotate around the y-axis, see *Fig. 1*, so that Eqs. [24b] and [25b] give:

$$V_{os} = \frac{\pi}{6} a^2 b \qquad [27]$$

The volume of a prolate spheroid V_{ps} is obtained by letting the ellipse in Eq. [24a] rotate around the x-axis (fig. 1), so that Eqs. [24a] and [25a] give:

$$V_{ps} = \frac{\pi}{6} a b^2 \qquad [28]$$

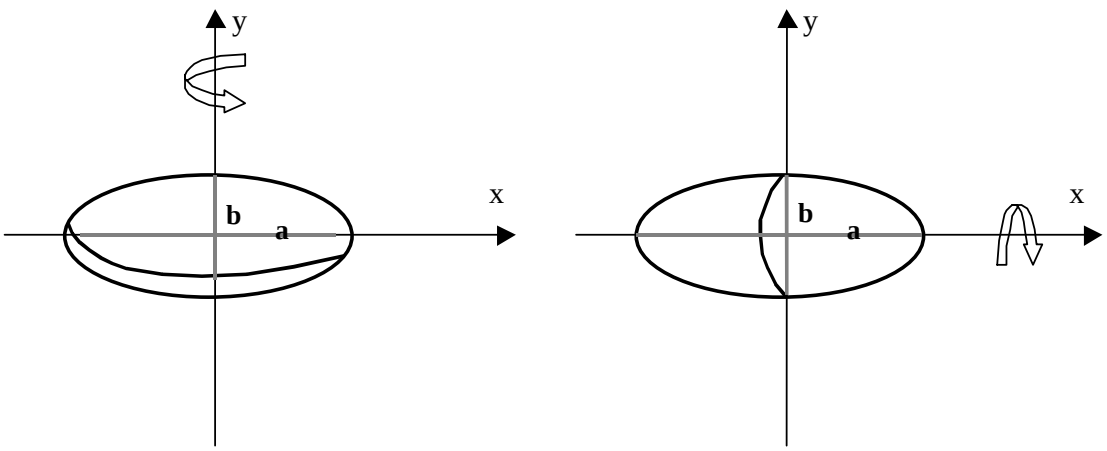

Fig. 1. The oblate spheroid is the body obtained by allowing an ellipse with major axis a and minor axis b to rotate around its minor axis (left), and the prolate spheroid is the body obtained by letting the same ellipse rotate around its major axis (right).

We define:

$$S = 2\pi \int f(x) \sqrt{1 + \left(\frac{df}{dx}\right)^2}\, dx \qquad [29a]$$

$$S = 2\pi \int f(y) \sqrt{1 + \left(\frac{df}{dy}\right)^2}\, dy \qquad [29b]$$

where S is the surface of revolution. The surface area of a sphere S_s is obtained from Eqs. [23] and [29a]:

$$S_s = \pi d^2 \qquad [30]$$

The surface area of an oblate spheroid S_{os} is obtained from Eqs. [24b] and [29b]:

$$S_{os} = 2\pi a^2 + \pi \frac{b^2}{e} \ln\left(\frac{1+e}{1-e}\right) \qquad [31]$$

where e is the ellipticity defined by:

$$e = \sqrt{\frac{a^2 - b^2}{a^2}} \qquad [32]$$

Similarly, the surface area of a prolate spheroid S_{ps} is obtained from Eqs. [24a] and [29a]:

$$S_{ps} = 2\pi b^2 + \frac{2\pi ab}{e}\arcsin e \qquad [33]$$

If for a given particle volume (arbitrary particle size of the sphere) S_{os}/S_s and S_{ps}/S_s are plotted against the aspect ratio, defined as a/b, we obtain *Fig. 2*:

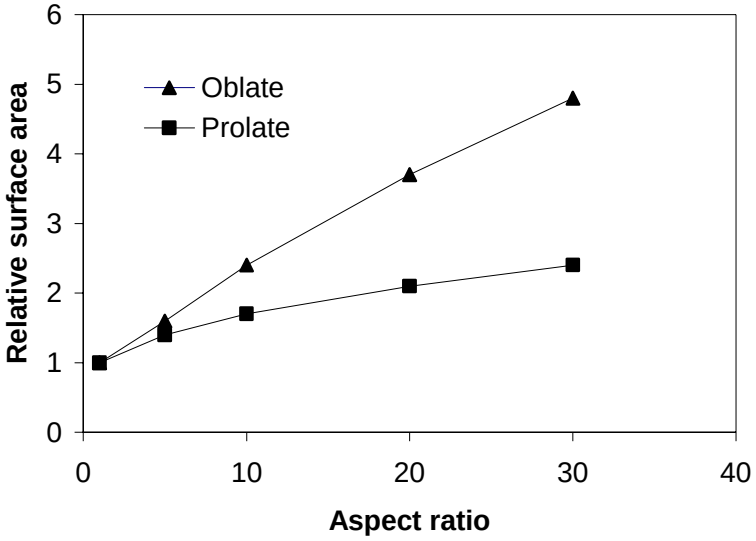

Fig. 2. Relative surface area for spheroids compared to that of a sphere with the same volume, as a function of the aspect ratio.

Fig. 2 shows that the relative surface area for an oblate spheroid increases almost linearly with increasing aspect ratio, whereas the corresponding curve for a prolate spheroid increases roughly logarithmically. At an aspect ratio of 30, the relative surface area of the oblate spheroid is about twice that of the prolate spheroid. Similar values (2.8) of the relative surface area are obtained at an aspect ratio of 10 for the prolate spheroid and 30 for the oblate spheroid.

Fig. 3 shows the major dimension a of a spheroid expressed in relation to the diameter d of a sphere of the same volume plotted against the aspect ratio.

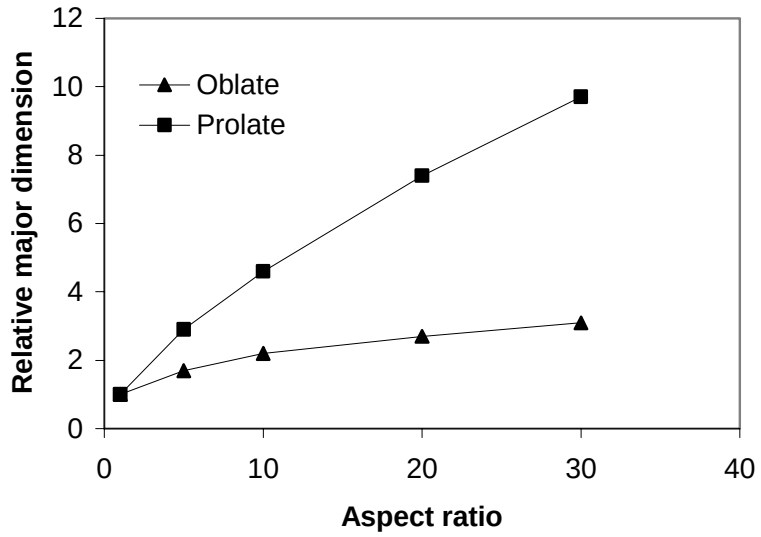

Fig. 3. Major dimension of a spheroid divided by the diameter of a sphere of the same volume plotted as a function of the aspect ratio.

Fig. 3 shows that the anisotropy of a prolate spheroid (defined as the major dimension of the spheroid to the diameter of a sphere of the same volume) increases almost linearly with increasing aspect ratio, whereas the corresponding curve for an oblate spheroid shows an almost logarithmic dependence. At an aspect ratio of 30, the relative major dimension is almost 10 for a prolate spheroid, but only about 3 for an oblate spheroid. This latter value is obtained for a prolate spheroid already at an aspect ratio of about 5.

In addition to these general trends, there is another very important relationship. If a particle is completely convex, like a sphere or a spheroid, the relationship between the surface area S and the average cross-sectional area in random orientation A is (Scarlett 1997):

$$\frac{S}{A} = 4 \qquad [34]$$

If the particle is not completely convex, then there is no simple relationship between the two parameters.

2.3 The packing of particles

The packing ability of monodisperse spheres, which is the simplest system that can be obtained, has been thoroughly investigated by Graton and Fraser (1935). In addition to the frequently occurring random systems (especially dense random packing with a density of 64 %), there are six orderly arranged packing systems, ranging from the cubic system with a solidity of 52 % to the rhombohedral system with a solidity of 74 %. This latter system is of interest in practice, as a maximum degree of compressibility will yield this structure, which is then given a priori. To indicate how complicated the packing of particles is already in the case of monodisperse spheres, it is remarkable that the rhombohedral system in turn consists of two different systems, the face-centred cubic and the hexagonal close packing. These two

systems have exactly the same solidity and the same number and sizes of the voids (a large octohedral and a small tetrahedral), but the inherent structure is different, and this has a great impact on the permeability. The fractional free area, A_f , is defined as the ratio of the free area of a plane parallel to the layers in regular packings to the total area of that plane. The ratio of the maximum to the minimum A_f is 1.6 for the face-centred system and 4.9 for the hexagonal close packing (Cumberland, Crawford 1987). Thus, despite the fact that the face-centred cubic and the hexagonal close packing systems are identical with respect to solidity, particle size, void size and number of voids per sphere, fluid flow through these packing systems will differ greatly.

For non-spherical particles, there are some trivial solutions of the packing problem. Mono-sized cubes may give a solidity of 100 %, and rods and discs of fixed size and a very high fixed aspect ratio may pack to a solidity of 90.7 % (Cumberland, Crawford 1987). The introduction of polydisperse size distributions and other particle shapes greatly increases the complexity of the packing problem. This is not surprising, since variables affecting the packing ability, to mention only a few, are particle shape, shape distribution, size distribution, methods of deposition, surface properties and elasticity (Cumberland, Crawford 1987). In filtration analysis, the concentration of the original suspension and the magnitude of the applied pressure may also be added as important parameters (Tiller et al. 1987).

Computer simulation as a tool to study particle packing has received increasing attention in recent years. Most of these studies seem to have been limited to the packing of spheres of different size distributions, e.g., log-normal, Gaussian, or Rosin-Rambler (Powell 1980; Suzuki, Oshima 1985; Soppe 1990; Konakawa, Ishizaki 1990; Reyes, Iglesia 1991). However, Hwang et al (1996) studied the two-dimensional packing of spheroids with various types of size distributions and standard deviations, but of fixed aspect ratio (= 2), in cake filtrations. The results were then transferred to three-dimensional structures by a statistical method. The most interesting result was that for all types of size distribution, the porosity was higher for spheroids than for spheres.

The packing of particles depends to a large extent on the order of magnitude of the particle size. For large particles, the ratio of the surface area to the volume is small and gravitational forces are large compared to colloidal forces (Tiller et al. 1987). Beds containing such particles are in general incompressible, as the particles become ”locked” in their initial positions. For small particles, roughly below 10 µm, both repulsive and attractive colloidal forces are large in comparison to gravitational effects, and such beds tend to be compressible as the particles become displaceable with respect to one another. Typical coating pigments with most of the particles below 2 µm (measured by a sedimentation technique) can therefore be expected to form compressible beds.

2.4 Particle size determination

Image analysis is the most appropriate way to estimate particle sizes and shapes. All dimensions of the particle can be measured, and if a sufficient number of particles is measured, good statistical precision is achieved. Image analysis is however time-consuming, tedious and expensive, and more rapid methods are required for routine analyses.

In particle size analysis using commercially avaliable instruments, it is common to interpret data in terms of the theory applicable to spherical particles. The dimension obtained is the ”equivalent spherical diameter” (ESD), which is the diameter of a sphere that would have the same behaviour as that recorded for the sample by the method in question. Hence, the ESD derived from the analysis of anisodiametric particles is not the same when different physical phenomena are taken as the basis of the measurement. Agreement is obtained only when spherical particles are encountered. For instance, a cylindrical particle of diameter 20 µm and length 60 µm will give an ESD of 33 µm if the particle volume is the basis of measurement (the Coulter Counter principle). In sieving, the particles pass through a 20 µm aperture and this method classifies them as 20 µm. Light scattering gives a result related to the cross-sectional area, and yields the largest ESD of these three methods.

Available size-determining methods, to mention a few, are: the Coulter Counter principle (the electrical sensing zone method), based on conductivity measurements; sedimentation, based on Stoke’s law (weight); light scattering, based mainly on laser diffraction; and photon correlation spectroscopy (dynamic light scattering), based on translatory diffusion due to Brownian motion. Commercial instruments are available for all these methods. The first two are mainly sensitive to the volume of the particle, whereas the latter two are mainly sensitive to the surface area or the average cross-sectional area. Photon correlation spectroscopy is mainly suitable for particle sizes below 0.2 µm, whereas the other methods should preferably be used for particles above this size. Two of the methods, light scattering and sedimentation analysis, will be more thoroughly described in the subsequent sections, since these were the methods used in this work.

2.4.1 Light scattering

The phenomenon of light scattering is different for large and small particles. If the particle is very large compared to the wavelength of the incident light, the optical properties of the particle are unimportant and scattering occurs solely through diffraction (the Fraunhofer theory). When the particle size is of the order of the wavelength of the radiation, the optical properties become important and the light is absorbed, refracted, reflected and diffracted. The particle shape is then also very important, which is not the case, however, if the particle size is very small compared to the wavelength of the radiation (Cadle 1965). The Rayleigh theory is then applicable, where the particle is considered to be in an oscillating electric field, which induces a corresponding electric moment in the particle. For spherical particles, a general theory, the Mie theory, covers the whole range of particle sizes. According to the Mie theory, the scattered light is the resultant of light waves originating from various parts of the particle, and the phase and the intensity of such waves are related in a highly complicated way. The Mie equation can be written in the form (Cadle 1965):

$$s_t = \frac{\lambda^2}{2\pi} \sum_{x=1}^{\infty} \left(\frac{q_x^2 + p_x^2}{2x+1} \right) \qquad [35]$$

where s_t is the total scattering by one spherical particle per unit intensity, and q_x and p_x are functions of d , the refractive index κ and the wavelength λ of the radiation. When s_t is divided by $\pi \frac{d^2}{4}$, the scattering per unit cross-sectionalal area of the particle s (the scattering coefficient) is obtained. Eq. [35] approaches Rayleigh scattering as the ratio $\frac{d}{\lambda}$ decreases, and Fraunhofer scattering as the ratio increases.

In laser diffraction instruments using a monochromatic light source, the interaction of the incident light beam and the ensemble of dispersed particles results in a scattering pattern with different light intensities at different angles. The total angular intensity distribution is then focused on a Fourier lens, which ensures that the scattering pattern that appears on the detector is independent of the location of the particles in the light beam (Cadle 1965). It is assumed that the recorded scattering pattern of the particle ensemble is equal to the sum of the patterns from all individual single scattering particles presented in random relative positions. To achieve this, the sample concentration should be very low (0.002 % by volume) and the overall scattering pattern should be sampled many times (about 1000). Finally, a deconvolution routine, incorporating the Mie theory and knowledge of the geometry and the sensitivity of the detector, is necessary to deduce the particle size distribution. This step is in fact the inverse of the calculation of a scattering pattern for a given particle size distribution. The detector is divided into sections, so that the particle size distribution is calculated in classes. The minimum detectable particle size depends on the size and location of the detector, but a common value is 0.1 μm.

Particle size measurements using light scattering usually provide some serious problems: firstly, the refractive index of the particles, especially the imaginary part connected to light absorption and surface roughness, is often not available and has to be chosen quite arbitrarily; secondly, the scattering pattern is circular only in the case of spherical particles (for anisometric particles, it is irregular and broadened); and thirdly, for broad size distributions, the fine-structure tends to be lost, as the minima and the maxima for different sizes will compensate each other, and this leads to a smoothing of the angular scattering pattern. However, the last problem is in part compensated for by including in the deconvolution algorithm mathematical procedures that contain some weighting of deviations between measured and calculated scattering patterns (e.g. least squares), some constraints (e.g. non-negativity for amounts of particles) and some smoothening of the size distribution curve (Cadle 1965).

2.4.2 Sedimentation

In sedimentation analysis, the transmittion of X-rays by a sample of suspended particles is measured as a function of time. The transmittance is related to the concentration of the particles. Stoke's law is assumed to be applicable, provided that the Reynold's number (defined in section 2.7) is less than 0.2. The terminal velocity is then assumed to be reached instantaneously and inertia terms are neglected (Allen 1981). The driving force downwards F_g is the gravitation such that:

$$F_g = m_p g - m' g = \frac{\pi}{6} d_v^3 (\rho_s - \rho_f) g \qquad [36]$$

where m_p is the mass of the particle, m' the mass of the same volume of fluid, g the acceleration due to gravity, d_v the volume ESD, ρ_s the density of the particle and ρ_f the density of the fluid.

In the opposite direction, a drag force F_D is acting, such that:

$$F_D = 3\pi\eta d_d \upsilon \qquad [37]$$

where d_d is the drag ESD and υ the velocity of the particle.

Since inertia terms are neglected, F_g and F_D must balance one another:

$$F_g = F_D \Rightarrow \upsilon = \frac{(\rho_s - \rho_g) g d_v^3}{18\eta d_d} = \frac{(\rho_s - \rho_g) g d_s^2}{18\eta} \qquad [38]$$

where d_s is the Stoke's diameter. It follows that

$$d_s = \sqrt{\frac{d_v^3}{d_d}} \qquad [39]$$

A successful sedimentation analysis therefore requires a reasonable difference in densities between the particles and the fluid, and a viscosity of the fluid that is not too high. In addition, the particle size must not be too small, as Brownian motion will then start to play a significant role. In fact, considering the densities of typical coating pigments dispersed in water, the distance travelled due to Brownian motion within a given time will exceed the distance travelled due to gravitation already at a particle size of 0.5 µm (Allen 1981). Nevertheless, the influence of Brownian motion at this particle size is very small as it occurs in all directions, whereas the movement due to gravitation is always a net effect straight downwards. However, the displacement due to Brownian motion will start to predominate greatly at a particle size of about 0.2 µm, and the analysis cannot be considered appropriate below this size for coating pigments dispersed in water. The typical cumulative sedimentation curve will level out at the fine end of the size distribution, indicating a significant influence of Brownian motion.

2.5 The aspect ratio

2.5.1 Flaky particles

The aspect ratio of flaky pigment particles like kaolin or talc is commonly defined as the ratio of the diameter across the face of the particle surface to the thickness. Thus, a higher aspect ratio means a flakier particle. A high aspect ratio is often considered beneficial for the smoothness of the coated paper, since the flaky particles are expected to be mainly aligned parallel to the paper surface, and for the printing properties, as the rate of ink vehicle absorption is reduced due to the high tortuosity, and more of the ink will remain on the paper surface. On the other hand, the flow properties are adversely affected by too high an aspect ratio of the pigment particles, as these may get stuck crosswise during flow resulting in a high viscosity of the coating colour. Sometimes runnability problems such as dilatancy, bleeding, streaks, web breaks etc will also arise. It is therefore clear that the aspect ratio of flaky pigment particles is a parameter of fundamental importance for the coating process. However, not only is the median or average value important but also the aspect ratio distribution as a function of particle size. This is analogous to the average particle size and the particle size distribution; the average particle size in itself is less important for the flow properties than the width of the size distribution. For instance, a broad particle size distribution means that the small particles can fill the voids between the larger ones, and this lowers the viscosity of the suspension at a given solids volume.

The aspect ratio of flaky particles is usually determined by image analysis, using a Transmission Electron Microscope and a shadowing technique to obtain the thickness of the particle (Morris et al. 1965). This method is however time-consuming, tedious and expensive, and more simple and rapid methods are required. Such methods can be based on conductivity measurements, light scattering analysis, low temperature calorimetry etc. (Baudet et al. 1996). However, no fully satisfying rapid method seems to have been developed yet. Most such methods evaluate only the average aspect ratio, and the aspect ratio *distribution* is neglected although it is also important.

2.5.2 Acicular particles

The aspect ratio of acicular (needle-shaped) pigment particles, like aragonite and satin white, is commonly defined as the ratio of the length to the diameter, and is thus a number greater than 1. Acicular particles have not received as much attention as flaky particles for two reasons: Firstly, they are much less frequently used as coating pigments, and secondly, a good approximation of the aspect ratio can be obtained from, e.g., two-dimensional Environmental Scanning Electron Microscopy (ESEM) images, as the major and one minor dimension of the particle will be in the x-y plane. Nevertheless, acicular particles are included in this work, as interesting features of coating layers based on such particles have been reported, especially a very high brightness compared to coating layers based on other PCC-grades (Engström, Rigdahl 1992).

2.6 The principal method

Fig. 4 shows ESEM images of kaolin and aragonite particles. Kaolin is flaky and aragonite is acicular, and these are the particle shapes considered in the principal method, which is a rapid

method to determine a shape factor and a shape factor distribution as a function of the ESD for pigment particles.

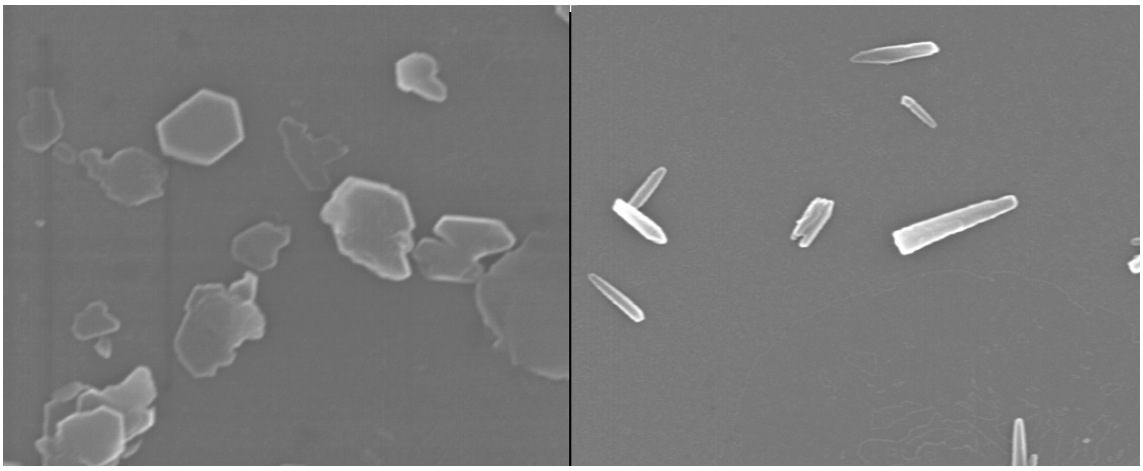

Fig. 4. Typical appearance of kaolin clay (left) and aragonite, PCC (right).

The kaolin particle (or e.g. talc) can be approximated as an oblate spheroid and the aragonite particle (or e.g. satinwhite) as a prolate spheroid (Jennings, Parslow 1988), see fig. 1. With these approximations, the three geometrical parameters of the particle are reduced to two, the major axis a and the minor axis b. The aspect ratio is defined as $r = \frac{a}{b}$. The oblate spheroid has two major axes, a, and one minor axis, b, whereas the prolate spheroid has two minor axes, b, and one major axis, a.

Based on the generalised geometries of oblate and prolate spheroids, the objective is now to obtain expressions for the ESD in terms of a and r (Jennings, Parslow 1988) when the pigment is studied by two basically different physical methods, namely light scattering and sedimentation.

The light scattering cross section of a sphere, A_{sp}, is given by:

$$A_{sp} = \frac{\pi d^2 s_{sp}}{4} \qquad [40]$$

where s_{sp} is the scattering coefficient (Bohren, Huffman 1983) of the sphere. The average light scattering cross section in random orientation of an oblate spheroid, A_{os}, is derived from Eqs. [31] and [34] (Slepetys, Cleland 1993):

$$A_{os} = s_{os} \frac{1}{8} \pi a^2 \{1 + [r\sqrt{(r^2 - 1)}]^{-1} \ln[r + (\sqrt{r^2 - 1})]\} \qquad [41]$$

where s_{os} is the scattering coefficient of the oblate spheroid.

Likewise, the average light scattering cross section in random orientation of a prolate spheroid, A_{ps}, is derived from Eqs. [33] and [34]:

$$A_{ps} = s_{ps}\pi r^2 \frac{1}{8r}\{\frac{1}{r} + \frac{r}{\sqrt{(r^2-1}}\arcsin[\frac{\sqrt{(r^2}-1)}{r}]\} \qquad [42]$$

where s_{ps} is the scattering coefficient of the prolate spheroid.

The light scattering ESD for an oblate spheroid, d_{lsos}, is obtained by equating [40] and [41]:

$$d_{lsos} = (\frac{a}{\sqrt{2}})\sqrt{1+[r\sqrt{(r^2-1)}]^{-1}\ln[r+(\sqrt{r^2-1})]} \qquad [43]$$

The light scattering ESD for a prolate spheroid, d_{lsps}, is obtained by equating [40] and [42], keeping in mind that $\arcsin[\frac{(r^2-1)}{r}] = \arctan[\sqrt{(r^2-1)}]$:

$$d_{lsps} = \frac{a}{\sqrt{2r}}\sqrt{\frac{1}{r} + \frac{r}{\sqrt{(r^2-1}}\arctan\sqrt{(r^2-1)}} \qquad [44]$$

The Stoke's ESD, d_s, is given by Eq. [39], where the volumes of a sphere, an oblate spheroid and a prolate spheroid, respectively, are given by Eqs. [26], [27] and [28], and where the drag ESD, d_d, is included in Eq. [38]. The drag force, F_d, can also be written (Allen 1981) as:

$$F_d = uf \qquad [45]$$

where f is the frictional coefficient of the particle, which for a sphere is $3\pi\eta d$ (Allen 1981). For an oblate spheroid moving with its minor axes parallel to the velocity vector, the frictional coefficient $f_{os,1}$ is (Happel, Brenner 1965):

$$f_{os,1} = 4\pi\eta\frac{a}{r}[\frac{1}{(r^2-1)} + \frac{(r^2-2)}{(r^2-1)^{1.5}}\arctan\sqrt{(r^2-1)}]^{-1} \qquad [46]$$

whereas motion with a major axis parallel to the velocity vector gives a frictional coefficient $f_{os,2}$:

$$f_{os,2} = 8\pi\eta a\{-\frac{r}{(r^2-1)} + \frac{(3r^2-2)r}{(r^2-1)^{1.5}}\arcsin[\frac{\sqrt{(r^2-1)}}{r}]\}^{-1} \qquad [47]$$

An average frictional coefficient for oblate spheroids, $\bar{f}_{os}$, can be calculated from:

$$\bar{f}_{os}^{-1} = \frac{1}{3}\sum_{i=1}^{3} f_{os.i}^{-1} \qquad [48]$$

with $i = 1,2,3$ for the three axes. This harmonic mean is often preferred when the surface area of the particle is concerned (Allen 1981), as it is closely related to the drag ESD. For an oblate spheroid, $f_{os,2} = f_{os,3}$ and, on the assumption that there is no preferential orientation in movement, Eqs. [46]-[48] yield:

$$\bar{f}_{os} = 3\pi\eta\frac{a}{r}\left(\frac{\sqrt{(r^2-1)}}{\arctan\sqrt{(r^2-1)}}\right) \qquad [49]$$

Eqs.[37], [45] and [49] give the drag ESD d_{dos} for an oblate spheroid:

$$d_{dos} = \frac{a\sqrt{(r^2-1)}}{r}\frac{1}{\arctan\sqrt{(r^2-1)}} \qquad [50]$$

The Stoke's ESD d_{sos} for an oblate spheroid is obtained from Eqs. [26], [27], [39], and [50]:

$$d_{sos} = a\sqrt{\frac{\arctan\sqrt{(r^2-1)}}{\sqrt{(r^2-1)}}} \qquad [51]$$

For a prolate spheroid moving with its major axes parallel to the velocity vector, the frictional coefficient $f_{ps,1}$ is (Happel, Brenner 1965):

$$f_{ps,1} = 8\pi\eta\frac{a}{r}\left\{\frac{(2r^2-1)}{(r^2-1)^{1.5}}\ln\left[\frac{r+\sqrt{(r^2-1)}}{r-\sqrt{(r^2-1)}}\right] - \frac{2r}{(r^2-1)}\right\}^{-1} \qquad [52]$$

and motion with a minor axis parallel to the velocity vector gives a frictional coefficient $f_{ps,2}$:

$$f_{ps,2} = 8\pi\eta\frac{a}{r}\left\{\frac{r}{(r^2-1)} + \frac{(2r^2-3)}{(r^2-1)^{1.5}}\ln\left[r+\sqrt{(r^2-1)}\right]\right\}^{-1} \qquad [53]$$

Eqs. [48], [52] and [53] give for prolate spheroids:

$$\bar{f}_{ps} = 3\pi\eta a\{\frac{\sqrt{(r^2-1)}}{r\ln[r+\sqrt{(r^2-1)}]}\} \qquad [54]$$

Eqs. [37], [45] and [54] give the drag ESD d_{dps} for a prolate spheroid:

$$d_{dps} = \frac{a\sqrt{(r^2-1)}}{r}\frac{1}{\ln[r+\sqrt{(r^2-1)}}} \qquad [55]$$

The Stoke's ESD d_{sps} for a prolate spheroid is obtained from Eqs. [26], [28], [39] and [55]:

$$d_{sps} = a\sqrt{\frac{1}{r\sqrt{(r^2-1)}}\ln[r+\sqrt{(r^2-1)}]} \qquad [56]$$

The working equation for an oblate spheroid is obtained by eliminating the major axis a between Eqs. [43] and [51]:

$$\left(\frac{d_{sos}}{d_{lsos}}\right)\sqrt{\frac{s_{os}}{s_{sp}}} = \sqrt{\frac{2r\arctan\sqrt{(r^2-1)}}{r\sqrt{(r^2-1)}+\ln(r+\sqrt{(r^2-1)})}} \qquad [57]$$

Eq. [57] can be solved using the algorithm given in appendix 1. This is basically an iteration process, described briefly as follows (Slepetys, Cleland 1993): The values of d_{sos} and d_{lsos} are given by the measurements; assume initially that s_{os}/s_{sp} = 1; calculate the left-hand side of Eq. [57] and extract r; calculate a from Eq. [56] and calculate the volume diameter $d_v = \frac{a}{r^{1/3}}$ (from Eqs. [26] and [27]); use this diameter to obtain s_{sp} (Bohren, Huffman 1983); use d_{lsos} to obtain s_{os} (Bohren, Huffman 1983); recalculate the left-hand side of Eq. [57] and continue the iteration until the result converges. In addition to Eq. [57], we define:

$$\left(\frac{d_{sos}}{d_{lsos}}\right) = \sqrt{\frac{2r\arctan\sqrt{(r^2-1)}}{r\sqrt{(r^2-1)}+\ln(r+\sqrt{(r^2-1)})}} \qquad [58]$$

i.e. Eq. [57] with the scattering coefficients omitted.

The working equation for a prolate spheroid is obtained by eliminating the major axis a between Eqs. [44] and [56]:

$$\left(\frac{d_{sps}}{d_{lsps}}\right)\sqrt{\frac{s_{ps}}{s_{sp}}} = \frac{\sqrt{\dfrac{\ln(r+\sqrt{(r^2-1)})}{r\sqrt{(r^2-1)}}}}{\sqrt{\dfrac{1}{2r}}\sqrt{\dfrac{1}{r}+\dfrac{r\arctan\sqrt{(r^2-1)}}{\sqrt{r^2-1}}}} \qquad [59]$$

Eq. [59] can be solved in a similar way to Eq. [57] using the corresponding equations for prolate spheroids and the algorithm given in appendix 2. In addition, we define:

$$\left(\frac{d_{sps}}{d_{lsps}}\right) = \frac{\sqrt{\dfrac{\ln(r+\sqrt{(r^2-1)})}{r\sqrt{(r^2-1)}}}}{\sqrt{\dfrac{1}{2r}}\sqrt{\dfrac{1}{r}+\dfrac{r\arctan\sqrt{(r^2-1)}}{\sqrt{r^2-1}}}} \qquad [60]$$

i.e. Eq. [59] with the scattering coefficients omitted.

If the right-hand sides $f(r)$ of Eqs. [57] (or [58]) for oblate spheroids and [59] (or [60]) for prolate spheroids are plotted against r, we arrive at *Fig. 5.* For a given aspect ratio, the quotient d_s / d_{ls} is larger for a prolate than for an oblate spheroid.

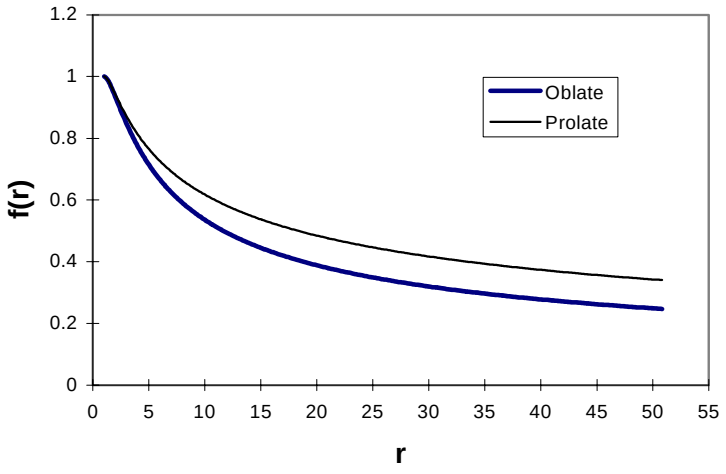

Fig. 5. The right-hand sides of Eqs. [57] and [59] plotted against r.

Eqs. [57] and [59] cannot be used directly to calculate aspect ratios for oblate and prolate spheroids for two reasons: firstly, the mathematical model applied in the principal method does not correspond exactly to reality, because a particle with three dimensions, i.e. length, width and thickness, cannot be exactly described using a model with only two parameters, a and b; and secondly, the scattering coefficients for oblate and prolate spheroids are calculated simply from the light scattering diameter using an algorithm for a perfect sphere, which usually yields too high scattering coefficients, at least for small light scattering diameters (for larger light scattering diameters, the optical properties of the particles become less important and finally the Mie theory may be replaced by the Fraunhofer theory). Properly, as pointed out by Slepetys and Cleland (1993), one must multiply the projected geometrical cross section in three principal directions by the corresponding light scattering coefficient and then average the result to obtain the adequate light scattering cross section. To overcome these shortcomings, the results must be corrected empirically.

A proposal for such a correction is to take the sum of the square root of r from Eq. [57] and the square root of r from Eq. [58] for flaky particles, and to use Eqs. [59] and [60] in a similar manner for acicular particles. The idea is as follows: consider flaky particles and Eq. [57], the original working equation. The light scattering coefficient is generally too high for small particles, and yields too small values of the aspect ratio. On the other hand, Eq. [58], where the scattering coefficients are omitted, gives too large values. Thus, some combination of these two equations might be used. Further, for small ratios, d_{sos} / d_{lsos}, r becomes unreasonably high. In fig. 5 the curves level out for small ratios, d_{sos} / d_{lsos}. It is therefore reasonable to use the square root of r, and the low number thus obtained is compensated for by the fact that we use the sum of two such square roots. This new number is best characterised as a shape factor, which is correct considering the definition of a shape factor (Allen 1981). To summarise, we define:

Shape factor (flaky particles) = $\sqrt{r}$ from Eq. [57] + $\sqrt{r}$ from Eq. [58] [61]

Shape factor (acicular particles) = $\sqrt{r}$ from Eq. [59] + $\sqrt{r}$ from Eq. [60] [62]

The principal method is better suited for the evaluation of shape factors for flaky than for acicular particles. This is because 1) the surface area of flaky particles increases more rapidly with increasing aspect ratio according to fig. 2, which means that there is a greater discrepancy between sedimentation and light scattering cumulative curves in a log-log diagram at a given aspect ratio (fig. 5), and 2) flaky coating pigments in practice have aspect ratios ranging from 5 to at least 50, whereas the aspect ratios of acicular particles are usually less than 10.

2.7 Rheology

The elastic or the viscous character of a material can be estimated (Barnes et al. 1989) through the Deborah number D_e:

$$D_e = \frac{t_c}{\chi_r} \qquad [63]$$

where t_c is a characteristic time (relaxation time) of the material and χ_r is a characteristic time of the deformation process being observed. If D_e<<1 the viscous character predominates, whereas if D_e>>1 the elastic character predominates. All materials can therefore behave in an elastic or viscous way depending on the time scale on which they are observed. A purely elastic material, within the linear viscoelastic region, behaves in accordance with Hooke's law, which means that the stress required to attain a given deformation is independent of the deformation rate. On the other hand, a purely viscous material behaves in accordance with Newton's law, which says that the stress is dependent only on the deformation rate, and is independent of the deformation itself. In the case of a coating colour subjected to a rather low shear rate, say 1000 s^{-1}, the viscous character will predominate clearly as the structure at rest is more or less broken down. At very high shear rates, >10^6 s^{-1}, such as those attained in the vicinity of the blade tip during blade coating, a partly elastic response is conceivable according to Eq. [63], since the blade thickness is less than 1 mm and the time of the deformation process is very short.

Another important number in rheology is the Reynold's number, R_e, which relates inertial forces to viscous forces:

$$R_e = \frac{v\rho_0 d}{\eta_0} \qquad [64]$$

where v is the velocity, ρ_0 the density and η_0 the shear viscosity of the fluid. Viscosity is defined only for laminar flow, i.e. R_e < ~2000. In capillary viscometry, the highest attainable shear rate is often limited by the critical Reynold's number ($R_e \approx 2000$).

2.7.1 The structure at rest

2.7.1.1 Viscoelasticity

The viscoelastic properties of a fluid can be evaluated by oscillatory measurements, or by performing creep or relaxation experiments (Barnes et al. 1989). All such methods are related to one another and provide similar information. Here, the focus is on oscillatory measurements, where the material is subjected to a sinusoidal stress τ at a certain frequency ω, and the responding strain γ or shear rate $\dot{\gamma}$ is measured:

$$\tau = G^*\gamma = \eta^*\dot{\gamma} \qquad [65]$$

where G^* is the complex shear modulus and η^* is the complex viscosity. Further,

$$G^* = G' + iG'' \qquad [66]$$

where G' is the storage modulus and G'' is the loss modulus. The complex viscosity can be written in a similar way. The elastic and the viscous parts of the response can be related to one another through a phase angle δ:

$$\tan\delta = \frac{G''}{G'} \qquad [67]$$

If δ is less than 45°, the elastic character predominates. It is important to realise that the elastic modulus determined pertains to a certain frequency and that, if the measurement is performed at another frequency, the elastic modulus will in general not be the same. Another important viscoelastic property is the strain at the end of the linear viscoelastic region, below which the storage modulus is independent of the deformation. This is an estimate of how large a deformation the structure can withstand before it starts to break down. The end of the linear viscoelastic region is sometimes defined as the point where the storage modulus has decreased by 10% of its original value.

2.7.1.2 Yield stress

Viscoelastic materials like coating colours do not have a true yield stress. The viscoelastic material will flow no matter how small a stress it is subjected to. However, in many situations the material will behave as though it had a yield stress, which may be called an ”apparent” yield stress. The apparent yield stress may be determined by subjecting the sample to an increasing stress and then measuring the stress at the local maximum in shear viscosity. In this case, for comparison purposes, it is important that different samples are subjected to measurements on similar time scales. Another way to estimate an apparent yield stress is to fit the Bingham equation to the flow curve (Barnes et al. 1989)

$$\tau = \tau_0 + \eta_{PL}\dot{\gamma} \qquad [68]$$

where τ_0 is the Bingham yield stress and η_{PL} is the plastic viscosity. The Bingham model indicates that the fluid has a yield stress, after which a Newtonian behaviour is observed. This is (apparently) true for coating colours in a limited region of the flow curve. Again, it is important for comparison purposes that the Bingham model is fitted in similar regions of the flow curves for different coating colours in order to achieve a fair comparison.

2.7.1.3 Intrinsic viscosity

It has been suggested (Lindhjem 1991) that the aspect ratio of pigment particles can be inferred from viscosity and solids content measurements using semi-empirical equations, such as the Dougherty-Krieger equation (Krieger, Dougherty 1959; Krieger 1972) and Eiler’s equation (Eiler 1941). These functional relationships have been applied over a wide concentration range and they have two features in common. Firstly, at very low concentrations they all reduce to the linear form

$$\frac{\eta_s}{\eta_0} = 1 + [\eta]\phi \qquad [69]$$

where η_s is the viscosity of the suspension, η_0 the viscosity of the solvent and $[\eta]$ the intrinsic viscosity. And secondly, at some characteristic volume fraction ϕ, the viscosity becomes infinite. Einstein (1906) found that $[\eta]$, defined as:

$$[\eta] = \lim_{\substack{\phi \to 0 \\ \dot{\gamma} \to 0}} \frac{\eta_r - 1}{\phi} \qquad [70]$$

where $\eta_r = \frac{\eta_s}{\eta_0}$, is precisely 2.5 for spheres, regardless of their size or size distribution. However, when non-spherical particles such as spheroids are in suspension, further complications arise owing to the rotation of these particles. The asymmetric particle does not rotate with a constant angular velocity, as would a spherical particle. Competition between the orienting tendency of the shear as measured by the shear rate and the rotational Brownian motion takes place. For a spheroid, the intrinsic viscosity can be written as a function of the aspect ratio $\frac{a}{b}$ (Jefferey 1923). Simha (1940) proposed the following expressions for "large" ratios $\frac{a}{b}$:

oblate spheroid $$[\eta] = \frac{(\frac{16a}{15b})}{\arctan\frac{a}{b}} \qquad [71]$$

prolate spheroid $$[\eta] = \frac{14}{15} + \frac{\left(\frac{a}{b}\right)^2}{5}\left(\frac{1}{3\ln\frac{a}{b} - 4.5} + \frac{1}{\ln\frac{a}{b} - 0.5}\right) \qquad [72]$$

Further, for prolate spheroids, Kuhn and Kuhn (1945) suggested the following expression for $1 \le \frac{a}{b} \le 15$:

$$[\eta] = 2.5 + 0.4075\left(\frac{a}{b} - 1\right)^{1.508} \qquad [73]$$

Eqs. [72] and [73] agree very well for $\frac{a}{b} > 5$. If Simha's both expressions hold for $\frac{a}{b} > 5$, then *Fig. 6* is obtained:

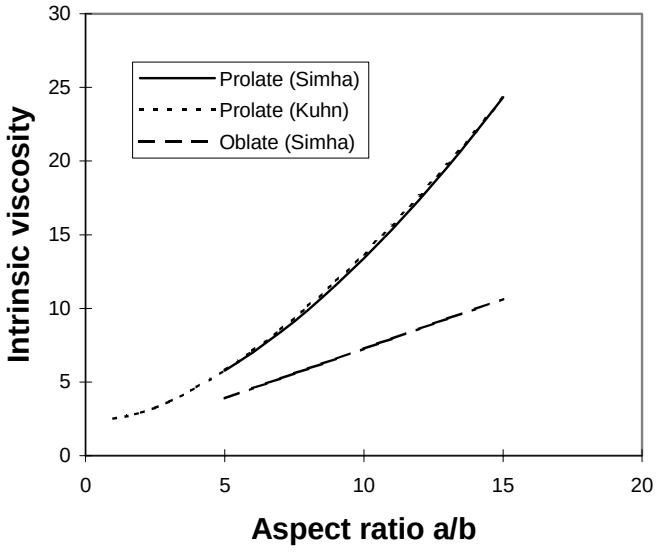

Fig. 6. Intrinsic viscosity versus a/b for Simha's expressions (Eqs. [70] and [72]) for oblate and prolate particles, respectively, and for Kuhn and Kuhn's expression for prolate particles (Eq. [73]).

Fig. 6 shows that the intrinsic viscosity of a suspension containing prolate spheroids increases almost exponentially with increasing aspect ratio, whereas the corresponding curve for a suspension containing oblate spheroids is linear. Since the product of the intrinsic viscosity and the maximum packing volume fraction is approximately constant (about 2 (Eiler 1941)), the packing ability of the particles will decrease according to the same relationships. It seems therefore that a linear increase in anisotropy (defined as ratio of the major dimension to the volume of the particle) with increasing aspect ratio corresponds to an exponential decrease in packing ability, and that a logarithmic increase in anisotropy corresponds to a linear decrease in packing ability (Figs. 2 and 6). However, these viscosity relations have so far been derived on the assumption that the concentration dependence of the viscosity can be neglected. For more concentrated systems, η_r can be expressed as a power series in ϕ (Frisch, Simha 1956):

$$\eta_r - 1 = 2.5\phi + c_1\phi^2 + c_2\phi^3 .... \qquad [74]$$

The coefficients $c_1, c_2 ...$ depend themselves on the shear rate and on the dimensions of the particle in suspension. Nevertheless, many attempts have been made to represent the concentration dependence of suspensions by empirical series in which the coefficients are treated as pure numerical constants, and many experimentally determined values of $c_1, c_2 ...$ have been suggested for different systems (Frisch, Simha 1956).

The η,ϕ data in the low and high shear rate regions were fitted by Krieger and Dougherty (1959), using a hard sphere suspension, which resulted in the following equation:

$$\eta_r = \left(1 - \frac{\phi}{\phi_m}\right)^{-[\eta]\phi_m} \qquad [75]$$

where ϕ_m is the maximum volume packing fraction, preferably determined by plotting ϕ against $\frac{1}{\sqrt{\eta_r}}$, followed by extrapolation to $\frac{1}{\sqrt{\eta_r}} = 0$. A prerequisite for Eq. [75] is that the interactions between pigment particles can be neglected, which is seldom true in practice. For instance, the presence of electrical charges on the spheres causes an augmentation of the intrinsic viscosity, because of increased energy dissipation in the electrical double layer surrounding the particle (Krieger 1972). Moreover, the viscosity should be independent of the shear rate. To attain this, the Bingham Eq. [68] is sometimes applied in a shear rate region where the shear viscosity is Newtonian.

2.7.2 Rheology at high shear rates

A focus in this work has been on the rheological behaviour of coating colours at high shear rates, i.e. at shear rates corresponding to those under the blade during blade coating. The reasons are that the flow situation is most complicated and interesting under the blade and that the shape factor evaluated by the principal method, described in section 2.6, is mass-based. The shape factor should therefore have its greatest relevance at high shear rates, where hydrodynamic forces predominate, rather than at low shear rates, where colloidal forces predominate which are partly unknown in these systems.

2.7.2.1 Capillary viscometry

The shear viscosity at high shear rates, > 100,000 s^{-1}, is usually measured by capillary viscometry. The fluid is then forced through a capillary of known dimensions under a given applied pressure, P, and the flow rate, Q, is measured. For Newtonian fluids, the Poiseuille equation is applicable and the flow profile is parabolic within the capillary (Barnes et al. 1989), and can be derived from the Navier-Stoke's equations, or simpler, from a one-dimensional analysis. Some corrections are however needed to properly estimate the shear viscosity in capillary viscometry (Willenbacher, Hanciogullari 1997). In the case of a Newtonian fluid, the pressure drop due to Newtonian entrance pressure losses (EPL), P_{ccN}, must be subtracted from the applied pressure. P_{ccN} is calculated as:

$$P_{ccN} = \frac{\rho_{su} d_c^2 \dot{\gamma}_{ca}^2}{64} \qquad [76]$$

where ρ_{su} is the density of the suspension, d_c the diameter of the capillary and $\dot{\gamma}_{ca}$ the apparent shear rate at the wall of the capillary. Eq. [76] is known as the Hagenbach-Couette (HC) correction or the kinetic correction. The total EPL for a non-Newtonian fluid, P_{cc}, must be determined experimentally through the Bagley plot. The applied pressure, P, is then plotted against the capillary length-to-diameter ratio for capillaries with similar diameters but

different lengths, at a constant shear rate. The straight line obtained is extrapolated and the interception with the P axis is an estimate of the EPL (Bagley 1957).
It follows that:

$$P_{cc} = P_{ccN} + P_{ccn} \qquad [77]$$

where P_{ccn} is the non-Newtonian part of the EPL (due to elasticity and/or additional elongational viscosity apart from that predicted for a Newtonian fluid according to Eq. [76] (Willenbacher, Hanciogullari 1997)).

The shear stress at the wall of the capillary, τ_c, is calculated as:

$$\tau_c = \frac{d_c(P - P_{cc})}{4L} \qquad [78]$$

where L is the capillary length.

The apparent shear rate at the wall of the capillary, $\dot{\gamma}_{ca}$, is calculated as:

$$\dot{\gamma}_{ca} = \frac{32Q}{\pi d_c^3} \qquad [79]$$

For a power-law suspension, the apparent shear rate is changed from the Newtonian value by a factor of $[3 + (1/n)]/4$, where n is the power-law index given by the power-law model

$$\eta = K \dot{\gamma}_{ca}^{n-1} \qquad [80]$$

where η is the shear viscosity and K the 'consistency' (Barnes et al. 1989). If log η is plotted against log $\dot{\gamma}_{ca}$, n is obtained from the slope of the straight line. This is known as the Rabinowitsch correction.

The shear viscosity, η, is calculated as:

$$\eta = \frac{\tau_c}{\dot{\gamma}_c} \qquad [81]$$

where $\dot{\gamma}_c$ is the shear rate at the wall of the capillary.

Another correction sometimes applied in capillary viscometry is for wall slip due to a migration of particles from the wall towards the centre of the capillary, which leads to too low an apparent viscosity of the sample. A Mooney-plot (Willenbacher, Hanciogullari 1997),

using capillaries of different diameters but similar diameter-to-length ratios, can correct for this phenomenon. The wall slip correction was however omitted in this work due to the difficulty of estimating proper viscosity values using this correction, cf. Carreau et al. (1992).

2.7.2.2 Slit die viscometry

In addition to capillaries, a slit die may be used at high shear rates to further evaluate the rheological behaviour of a fluid (Tsuji et al. 1990). The slit die has a rectangular geometry and, in general, a narrow gap size compared to the diameter of a capillary, see *Fig. 7*, so that the EPL will in most cases predominate in the flow resistance in a slit die.

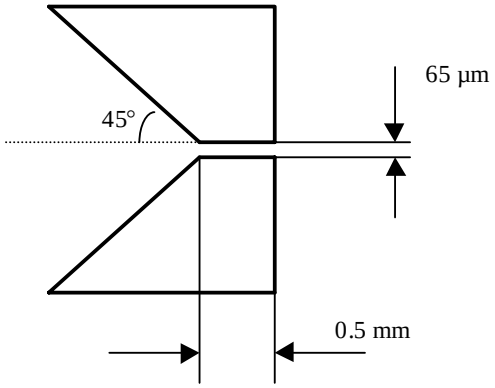

Fig. 7. Dimensions of the slit die used in this work.

Fig. 7 shows also that the shearing distance in the gap (0.5 mm) is similar to the thickness of a blade during blade coating. Since the geometry of the slit die and the time-scale of shearing are similar to the conditions in the vicinity of the blade tip during blade coating, the slit die is expected to provide a better correlation with runnability compared to capillary viscometry. However, it should be borne in mind that the situation during blade coating is still quite different. For instance, during blade coating, the flow is mainly velocity driven (rather than pressure driven as in slit die viscometry), a compressible and water-absorbing base paper is present beneath the blade and, in particular, about 90 % of the colour is recirculated at all times. Nevertheless, interesting features appear using the slit die, especially the pronounced impact of non-Newtonian effects, which are difficult to study using capillaries alone. Such effects may have a dramatic influence on the flow behaviour of coating colours, as has been shown by previous modellings and experiments using model solutions (Sullivan, Middleman 1986; Ohlsson, Isaksson 1995), as well as on the final properties of the coating.

The EPL for a Newtonian fluid in a slit die, P_{csN}, is calculated (Whorlow 1992) as:

$$P_{csN} = \frac{0.8\rho \dot{\gamma}_{sa}^{\,2} h_s^{\,2}}{36} \qquad [82]$$

where $\dot{\gamma}_{sa}$ is the apparent shear rate at the wall and h_s is the height of the slit.

Also,

$$P_{cs} = P_{csN} + P_{csn} \qquad [83]$$

where P_{csn} is the non-Newtonian contribution to the EPL for a slit.

For a slit die, an additional correction, Couette (Whorlow 1992), is needed due to the fact that stable flow conditions are not attained immediately within the gap, but after a certain distance which is approximately equal to the height of the slit. The effective length of the slit, l', is therefore defined as:

$$l' = l + h_s \qquad [84]$$

where l is the length of the slit die. This correction is not necessary for a capillary, as the diameter is then negligible compared to the length.

The shear stress at the wall of the slit die, τ_s, is:

$$\tau_s = \frac{h_s (P - P_{cs})}{2l'} \qquad [85]$$

The apparent shear rate is calculated as:

$$\dot{\gamma}_{sa} = \frac{6Q}{w h_s^{\,2}} \qquad [86]$$

where w is the width of the slit.

The shear viscosity in the slit is:

$$\eta = \frac{\tau_s}{\dot{\gamma}_{sa}} \qquad [87]$$

The Rabinowitsch correction should be avoided in slit die viscometry, since it may give rise to large errors (Mäkinen 1999). The effect of the Rabinowitsch correction is however small at least in capillary viscometry, whereas corrections for the EPL are always important. Pressure losses at the exit of the slit die and the capillary were considered negligible in this work, as they are usually small compared to the corresponding EPL (Binding 1998).

2.8 Pore structures

When the coating colour applied to the paper surface is dried, using hot-air and IR-dryers, a first critical concentration is reached when the pigment particles are brought into contact with one another, and a matrix is formed. The fluid phase is however still mobile, and the structure may shrink until the second critical concentration is reached, after which the latex has sometimes formed a film and then no longer exists as separate particles. The amount of latex included should be sufficient to yield a high mechanical strength of the coating layer, but it should not fill the voids between the pigment particles, as this would reduce the porosity of the coating layer. The pore structure, which is important for most properties of the coating layer such as the brightness, the opacity, and the absorption of ink vehicle, is related to the packing ability of the particles. Other factors affecting the pore structure are the coating colour formulation, the application technique, the machine speed, the drying conditions and the base paper. The pore structure of a coating layer can be evaluated by different methods, such as image analysis, mercury porosimetry (Kettle, Matthews 1993), NMR cryoporometry (Furó, Daicic 1999) and ink-tack measurements (Gane, Seyler 1994). Mercury porosimetry, based on the principle that the applied intrusion pressure is inversely proportional to an equivalent diameter of the void, has been the most popular method in recent years, possibly due to the fact that it is rapid, simple and not too costly. However, the major drawback of this metod is that the measured pressure is related to the narrowest part of the pore (the “neck” or the “throat”). It can therefore be suspected that the pore diameters determined by mercury porosimetry are too small, as was shown for clay structures by Climpson and Taylor (1976). In addition, the compressibility of the sample may be an important factor at very high pressures (Gane et al. 1996). Evaluations by mercury porosimetry should therefore be used for ranking different samples, rather than for estimating absolute values.

Modelling of pore structures is sometimes based on the assumption that the overall void network can be replaced by a number of similar and parallel capillaries (in Bristow, Kolseth 1986). The Poiseuille equation may be used to characterise the flow through the capillaries and, with the introduction of a driving force due to surface tension (the Young-Laplace equation), the Lucas-Washburn relationship for absorption can be derived (in Bristow, Kolseth 1986). The liquid permeability may be calculated from the Kozeny-Carman relationship (Coulson, Richardson 1978). The drawbacks of this approach are that the model geometry is extremely simple and that inertial terms are neglected.

The Pore-Cor model (Kettle, Matthews 1993) is considered to be an improvement on traditional mercury porosimetry. Pore-Cor is fitted to the experimental data obtained by this method, and the computation is based on the assumption that the real void structure can be replaced by a bundle of capillaries (throats) and cubes (voids) of different sizes (Kettle, Matthews 1993; Matthews et al. 1995). Pore-Cor uses a percolation algorithm which is considered to have some advantages over the experimental data obtained by mercury porosimetry, e.g. Pore-Cor takes into account the fact that larger pores may be shielded by smaller ones during liquid intrusion. Further, some properties of the coating layer can be estimated through this model that are difficult to measure experimentally, e.g. a Darcian liquid permeability (Gane et al. 1996). However, the limitation of a rather simple geometry to map the void network still remains.

2.9 Statistics

The particle size distributions as well as the aspect ratio distributions seem to be approximately log-normal for commercial samples of clay and talc (Aitchison, Brown 1969; Ojala 1976). However, artificially manufactured samples of precipitated aragonites do not always follow this relationship (Ojala 1976).

If a distribution is log-normal, it is easy to make statistical estimations of confidence intervals using the Gaussian distribution and the logarithms of the values. For a confidence limit of, say, 95 % the measured parameter will fall in the range:

$$\bar{x}_n \pm \frac{1.96\sigma}{\sqrt{\psi}} \qquad [88]$$

where $\bar{x}_n$ is the number-based geometric mean value (= median value), σ is the geometric standard deviation, 1.96 is the 0.975-fractile in the Gaussian distribution and ψ is the number of observations.

In general, if a number distribution of a certain parameter obeys a given distribution law, the mass distribution does not. According to Allen (1981), this is not the case for the log-normal distribution. If a number distribution is log-normal, the mass distribution is also log-normal with the same standard deviation. Conversion from one distribution to another is then easy using the following relationship (Allen 1981):

$$\log \bar{x}_n = \log \bar{x}_m - 6.9 \log^2 \sigma \qquad [89]$$

where $\bar{x}_m$ is the mass-based geometric mean value.

However, this relationship cannot be always valid in the case of aspect ratio measurements, as a very high aspect ratio may be related to a small particle volume. Eq. [89] should therefore not be used if aspect ratios are the subject of investigation.

3. Experimental

3.1 Materials

All the pigments used in this work are listed in Table 1.

Table 1. Data for pigments

Pigment	Trade Name	Shape	Median size[1] (µm)	Width of size dist.[2]	Manufacturer
kaolin	Speswhite	flaky	0.60	2.50	ECC[3]
kaolin	Supreme	flaky	0.46	1.55	ECC
kaolin	Amazon 90 SD	flaky	0.23	0.91	CADAM[4]
kaolin	Kaofine 90	flaky	0.20	0.92	TKC[5]
kaolin	Kaovit	flaky	0.56	2.30	TKC
kaolin	Nuclay	flaky	0.48	2.08	Engelhard[6]
kaolin	"Fraction A"[7]	flaky	0.29	0.62	ECC
kaolin	"Fraction B"[8]	flaky	0.77	0.43	ECC
kaolin	"Fraction C"[9]	flaky	1.95	0.51	ECC
talc	Finntalc C10	flaky	2.40	1.43	Finnminer.[10]
aragonite	Opacarb A40a (PCC)[11]	acicular	0.39	0.77	Specialty[12]
aragonite	Opacarb A40b (PCC)[11]	acicular	0.39	0.77	Specialty
aragonite	Opacarb A60a (PCC)[11]	acicular	0.62	1.20	Specialty
aragonite	Opacarb A60b (PCC)[11]	acicular	0.62	1.20	Specialty
aragonite	Opacarb A80 (PCC)	acicular	0.76	1.13	Specialty
aragonite	Opacarb mix (PCC)	acicular	0.56	1.09	Homemade[13]
polystyrene	DPP 722E	spherical	0.45	0 (monod.)	Dow[14]
polystyrene	DPP 711	spherical	0.26	0 (monod.)	Dow
polystyrene	XZ 95065	spherical	0.11	0 (monod.)	Dow
silica colloid	"Stöber sols"	spherical	0.28	0.68	Chalmers[15]

1. Median equivalent spherical diameter measured by a Sedigraph (based on wt%), except for the polystyrene pigments.
2. Calculated as $(D_{75}- D_{25})/ D_{50}$ from a Sedigraph curve (based on wt%), except for the polystyrene pigments.
3. English China Clay International Ltd., England
4. Caulim da Amazônia S.A., Brazil
5. Thiele Kaolin company, GA, USA
6. Engelhard corp., GA, USA
7. Particle size (sedimentation) < 0.5 µm.
8. Particle size (sedimentation) 0.5 – 1.0 µm.
9. Particle size (sedimentation) 1.5 – 2.5 µm.
10. Finnminerals Oy, Finland
11. Two grades of each of the pigments Opacarb A40 and Opacarb A60 were used. The particle size distributions (sedimentation) were similar, but the aspect ratios differed.
12. Specialty Minerals Oy, Finland
13. Obtained by mixing 2/3 Opacarb A80 and 1/3 Opacarb A40a, by weight.
14. Dow Rheinmünster GmbH, Germany.
15. Department of Engineering Chemistry, Chalmers University of Technology, Sweden.

The water-soluble polymers used were carboxymethyl cellulose (CMC) of three different molecular weights: 45 kg/mole (CMC FF5); 66 kg/mole (CMC FF10); and 115 kg/mole (CMC FF150). These were supplied by Metsä-Serla Oy, Finland. In addition, a polyacrylamide (PAM) with an average molecular weight of 3.3×10^3 kg/mole was used (Percol 155 from Allied Colloids Ltd, England). Sodium polyacrylate (Dispex N 40 from Allied Colloids Ltd, England) was used as additional dispersant for the clay pigments. A carboxylated styrene-butadiene latex (DL 935 from Dow Rheinmünster GmbH, Germany), with a diameter of 0.15 µm, was used as binder.

3.2 Instruments

The laboratory equipment used in this work is listed in Table 2.

Table 2. Laboratory instruments used.

Instrument	Measured property (or purpose)
Sedigraph 5000	Particle size based on sedimentation
Mastersizer 1000	Particle size based on light scattering
Atomic Force Microscopy (AFM)	Particle shape and size, including thickness
Environmental Scanning Electron Microscopy (ESEM)	Particle shape and size
Stresstech rheometer	Rheological properties at low shear rates
Bohlin VOR	Rheological properties at low shear rates
Capillary viscometer	Rheological properties at high shear rates
Slit die viscometer	Rheological properties at high shear rates
ÅA-GWR	Water retention capacity (filtration)
Home-made pressure filtration device	Water retention capacity (filtration)
GE Signa Horizon 1.5 T	Water content (magnetic resonance imaging)
Bench coater (K-coater)	Coating (low shear rates)
Cylindrical laboratory coater (CLC)	Coating (high shear rates)
Mercury porosimeter Autopore III	Pore structure, porosity
IGT AIC2-5	Surface strength
Datacolor Elrepho 2000	Reflectance, opacity, brightness
ZLR 1050 Zehntner	Gloss (Lehmann)
L&W PPS Tester	Surface roughness (PPS-10)

3.3 Coating colour preparation

A clay pigment received as powder was dispersed in water containing the dispersing agent and sodium hydroxide under high shear for 30 min under the conditions suggested by the manufacturer. The pigment-only suspension thus obtained was of a high solids content, typically about 70 % (by weight), and the particles were assumed to be well separated. The amount of dispersing agent added was typically less than 0.5 pph (parts per hundred parts of pigment, by weight). The addition of sodium hydroxide was even less, to obtain a pH-value in the slurry of about 8.5. Polystyrene, silica and aragonites were always supplied as predispersed slurries.

To obtain a coating colour, a water-soluble polymer (usually CMC) in a solution and latex were added slowly to the pigment-only suspension under gentle stirring. The amount of CMC added (when applied) was typically 1 pph or less, and the amount of latex added (when applied) was 10 pph. The final solids content was then adjusted to about 60 %. The coating colours were left to equilibrate at room temperature for 24 h before any measurement was made. The final pH-value was adjusted to about 8.5.

3.4 Coating

A coating was produced by applying the coating colour to a substrate such as polyethylene film (bench coating, low shear rates) or a base paper (cylindrical laboratory coating (CLC) or pilot plant coating, high shear rates). The coating layer thus obtained was dried in an oven at 105 °C in the former case, or using hot-air and IR-dryers in the latter. The coat weights attained were typically 80 g/m^2 (bench coating) and 10 g/m^2 (CLC or pilot plant coating).

4. Results and discussion

4.1 Spherical particles

4.1.1 Dewatering

The dewatering behaviour of model coating dispersions was investigated under static conditions in the laboratory. Using monodisperse spherical polystyrene particles at a 48 % solids content initially, filtration experiments were performed at a constant pressure of 50 kPa. The filtration experiments were non-invasively monitored by a rapid MRI technique (Magnetic Resonance Imaging), which is non-destructive, and by which the water content at different z-positions can be measured. In *Fig. 8* it can be seen that a solidity gradient appeared in the suspension nearest the filter (the filter cake) during dewatering. The solidity of the cake at the filter medium was 71 % after 480 s, which indicated a higher solidity than that of randomly packed monodisperse spheres, which is 64 %. With a resolution of the measurement of 0.8 mm, there may well have been a layer of close packed spheres just above the filter, which would correspond to a solidity of 74 %.

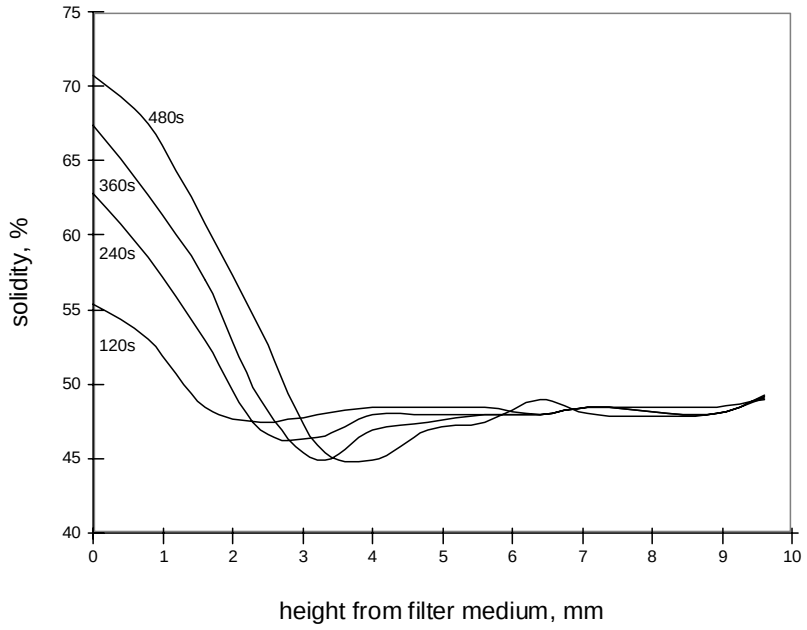

Fig. 8. Solidity profiles for a polystyrene-only dispersion against height from the filter medium at different times during dewatering (Paper I).

A concentration gradient as depicted in fig. 8 is not accounted for in traditional coating theory (Letzelter 1997). The mathematical model presented in section 2.1 was fitted to the experimental data, and a good agreement was obtained, as can be seen in *Fig. 9* for a pigment-only suspension (top) and for a suspension containing water-soluble polymer (bottom). The results are presented in scaled form, which means that the scaled solidity at the filter as well as the scaled height of the cake are 1.0 in all cases. According to the theory, the scaled

gradient is the same at all times, indicating that the very long time-scale used (480 s) is irrelevant – the scaled gradients seen in fig. 9 are present from the beginning and throughout the experiments. The constant α in Eq. [22], related to the concentration gradient, was found to be 0.26 in the the case of the pigment-only suspension, and 0.16 in the case of the suspension containing CMC. The scaled gradients are probably the same regardless of particle size for monodisperse spheres (for small particles where colloidal forces predominate over gravitational forces), as was shown in paper I.

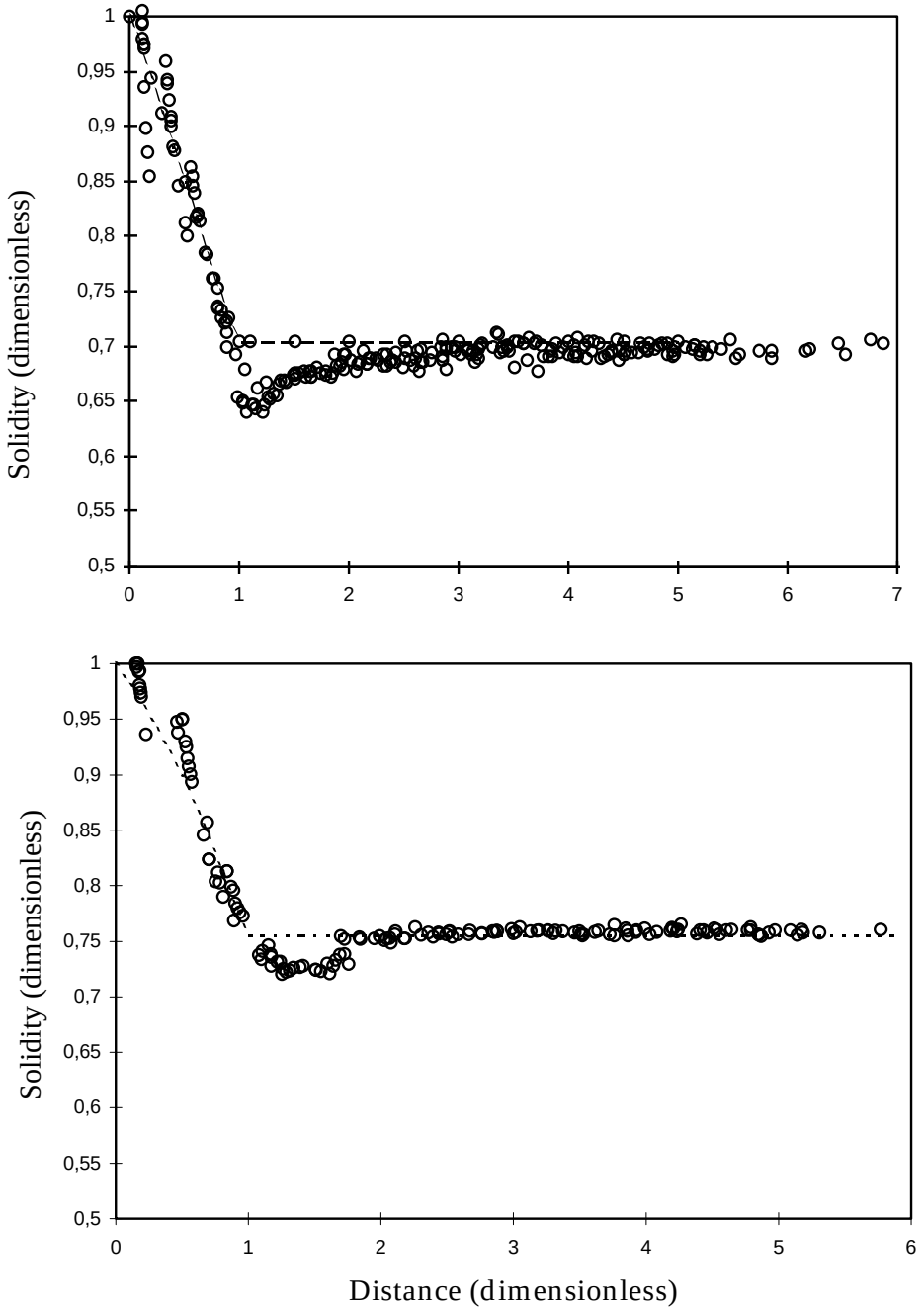

Fig. 9. Comparison of theoretical (dotted line) and experimental solidity profiles for a polystyrene-only suspension (top) and a suspension containing 0.8 pph CMC FF5 (bottom). Dimensionless parameters on both axes (Paper I).

The local minimum in solidity just above the filter cake observed in the MRI experimental results (see also fig. 8), is however not seen in the simulated data. In fact, here, the solidity appears to be lower than in the original dispersion. The discrepancy between the experimental observation and the simulation remains to be explained. A possible explanation is that there is some kind of discontinuity at the boundary between cake and dispersion, e.g. in magnetic susceptibility. Such discontinuities may give rise to artefacts. For instance, it is well-known that the Fourier series (the response signal is converted from a time domain to a frequency domain) does not converge uniformly to a discontinuous function in an arbitrarily small interval of the discontinuity point, the so-called Gibbs phenomenon. However, such artefacts should not affect the appearances of the gradients themselves in figs. 8 and 9.

4.1.2 The principal method

According to the principal method outlined in section 2.6, the two cumulative size distributions from light scattering and sedimentation methods will theoretically coincide only if spherical particles are encountered. This was also found to be the case for a bimodal distribution of silica spheres, as shown in *Fig. 10*, except for the fine end of the distributions. The major reason for this discrepancy is probably Brownian motion during sedimentation. This phenomenon should be less pronounced for clay and calcium carbonate pigments, as the densities of these pigments are higher (2.6-2.9 compared to 2.2 g/cm^3 for silica), and the influence of gravitational forces is therefore stronger.

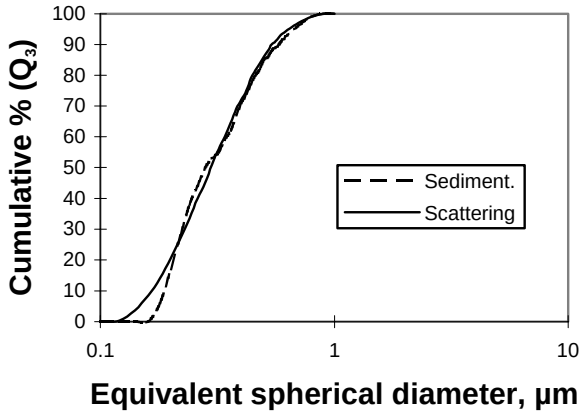

Fig. 10. Cumulative mass-based (sedimentation) and volume-based (light scattering) particle size distributions (Q_3) for silica spheres of mean size 275 µm (Paper II).

4.1.3 Rheology

4.1.3.1 Intrinsic viscosity

The intrinsic viscosity of suspensions containing the silica pigment, evaluated using the Dougherty-Krieger Eq. [75], was 2.9, and the corresponding value for suspensions containing the polystyrene pigment was 2.6. These values are quite close to the theoretical value of 2.5 (see section 2.7.1.3). The reason for the greater discrepancy in the case of silica particles was

probably that the concentrations of these suspensions were rather low, which means that the fitting to the Dougherty-Krieger relationship had to be carried out far from the immobilisation point of the suspension.

4.2 Flaky and acicular particles

4.2.1 Image analysis and statistics

The results of image analyses on some clay and aragonite pigments are shown in *Table 3.*

Table 3. Results of image analysis (Paper II).

Trade name	Number of particles observed	Major dimension[1] (by number) µm	Mean of[2] $2xD_{min}/(D_{max}+D_{min})$	Confidence interval[3], ±% of major dimension	Mean aspect ratio[4] (by number)	Corresponding equivalent sph. diameter[5] µm
Speswhite	210	0.45	0.85	5	16.0	0.18
Amazon	200	0.37	0.88	5	8.2	0.18
Kaovit	216	0.32	0.87	4	11.3	0.14
Opacarb A40a (PCC)	334	0.59		7	1.9	0.39
Opacarb A60a (PCC)	509	0.79		5	2.6	0.42
Opacarb A80 (PCC)	362	1.03		6	3.2	0.48

1. Geometric mean.
2. Arithmetic mean.
3. A log-normal distribution is assumed, which was found to agree well with the particle size distributions of the measured particles. Confidence limit = 95%. The 0.975-fractile (=1.960) in the Gaussian distribution has been used, which is a permissible approximation to the Student's t-distribution for large values of n (n>100).
4. Geometric mean.
5. Oblate or prolate model applied to calculate the volume of the particle; $V_{oblate}= \pi a^2 b/6$; $V_{prolate}= \pi a b^2/6$.

The particle size distributions as well as the aspect ratio distributions were found to be approximately log-normal (the log-normal distribution is well established in small particle statistics (Aitchison, Brown 1969)), which means that these distributions are best characterised by their geometric means (= medians) rather than by their arithmetic means. The interval estimations resulted in confidence intervals of between ±4% and ±7% for the major dimensions for all pigments (confidence limit 95%), showing a good accuracy of the image analysis, although a rather small number of particles has been measured.

Table 3 shows that the aspect ratios (length to width ratio) of the acicular particles were very low. Speswhite had the highest aspect ratio amongst the flaky particles, 16.0, followed by Kaovit, 11.3, which was a surprisingly low value for a delaminated clay. On the other hand, these are the number-based distributions, which in general differ a lot from the mass-based distributions. It can also be seen in table 3 that the Speswhite particles were much larger than the Kaovit particles (with respect to number distribution).

Further, in table 3 it can be seen that D_{min} across the face of the particle surface amounted to between 85 % and 88 % of the arithmetic mean of D_{min} and D_{max} for the flaky particles, or in other words, that D_{min} amounted to between 75 % and 79 % of D_{max}. Apparently, the oblate

spheroid model used in the principal method, which assumes that D_{min} and D_{max} are equal, is a rather rough approximation.

4.2.2 The principal method

The cumulative sedimentation and light scattering curves for some of the coating pigments are shown in *Fig. 11*. These distributions are mass(volume)-based, and the horizontal distance between the sedimentation and the light scattering curves indicates the shape factor of the particles. In general, a shorter distance can be expected between the light scattering and sedimentation curves for acicular than for flaky particles for a given value of r, see fig. 2.

It can be seen in fig. 11 that Speswhite and Kaovit were similar in shape, and that Kaovit had the highest shape factor. The shape factors of these pigments increased with increasing particle size up to a certain cumulative point, after which they decreased again. The curves for Amazon and Kaofine also had similar shapes and these pigments apparently had much lower shape factors than Speswhite and Kaovit. The trend was also different for Amazon and Kaofine, where the shape factor continously increased with increasing particle size, especially for Kaofine. For talc, a maximum shape factor was noted at a cumulative particle size of about 10%, indicating that the number-based aspect ratio was higher than the mass-based shape factor. This may be a bit surprising, but it seems to be confirmed by the results obtained by Ojala (1976), where it was indicated that the high aspect ratio of Finntalc C10 is due mainly to the very thin particles at the fine end of the size distribution. The acicular particles (PCC) all exhibited low aspect ratios, but these curves cannot be compared to those for flaky particles, because different working equations have been applied for flaky and acicular particles. For Opacarb A40a, the aspect ratio appeared not to depend significantly on the particle size, whereas for Opacarb A60a and Opacarb A80 a clear dependence can be observed.

Table 4 shows the median shape factors and the mean aspect ratios of each pigment obtained by image analysis for those particles that are lying approximately at the median ESD according to the principal method. The same trends can be observed. For the acicular particles, however, the aspect ratios were low without exception, with respect to both a number distribution and a mass distribution, which resulted in a somewhat poor evaluation of the aspect ratio for this pigment.

Table 4. Comparison between the results from image analysis and the principal method (Paper II).

Trade name	Aspect ratio from image analysis (number-based)	Aspect ratio[1] from image analysis (mass-based)	Shape factor (mass-based)
Speswhite	16	19	20
Amazon	8	10	5
Kaovit	11	25	30
Opacarb A40a (PCC)	2	2	4
Opacarb A60a (PCC)	3	4	6
Opacarb A80 (PCC)	3	4	5

1. Calculated for those particles that had approximately the median ESD according to the principal method.

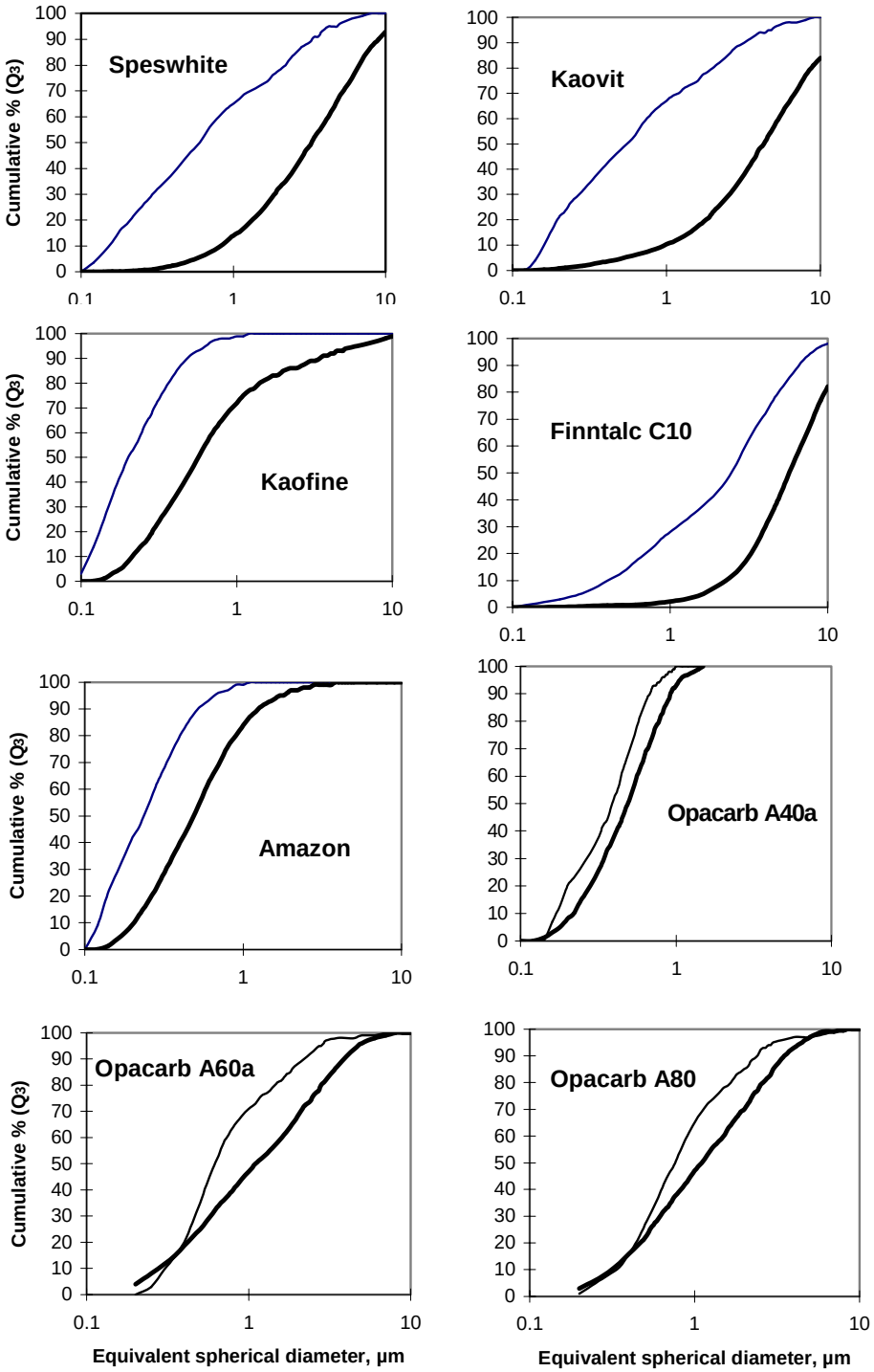

Fig. 11. Cumulative mass-based (sedimentation) and volume-based (light scattering) particle size distributions (Q_3), for Speswhite, Kaofine, Kaovit, Amazon, Finntalc C10, Opacarb A40a, Opacarb A60a and Opacarb A80. Thin line: sedimentation; thick line: light scattering (Paper II)

Fig. 12 shows the shape factors of some of the pigments as a function of the equivalent Stokes diameter from 20 to 80 % in pigment quantity.

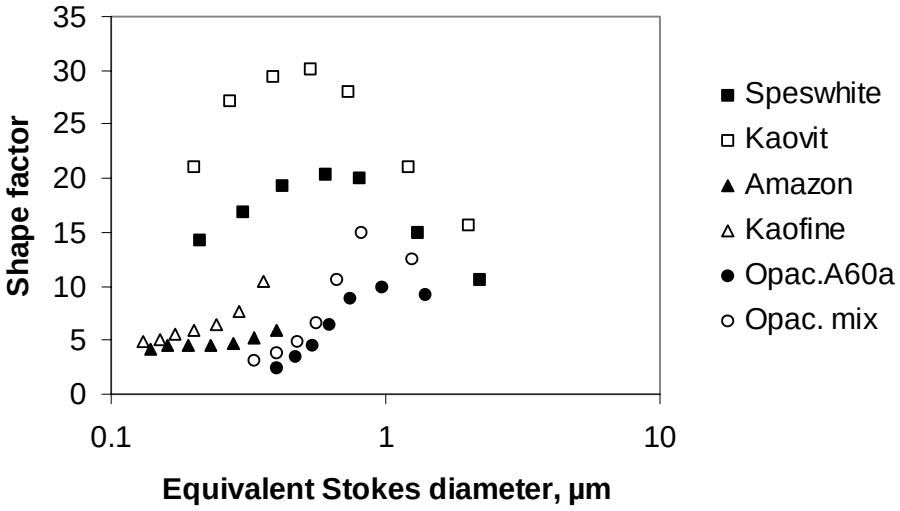

Fig. 12. Shape factor versus equivalent spherical diameter (sedimentation) for some pigments from 20 % to 80 % in cumulative pigment quantity (Paper III).

In addition, it can be mentioned that another delaminated clay, Nuclay, had a median shape factor of 36 and that the shapes of the cumulative curves were quite similar to those of the other delaminated clay, Kaovit. Two other aragonites, Opacarb A40b and Opacarb A60b, have also been used, and these had aspect ratios different from those of their counterparts, Opacarb A40a and Opacarb A60a, respectively. These pigments, listed in *Table 5*, are those that are subsequently used in this work for evaluations of rheological properties of coating colours and properties of coating layers.

Table 5. Data for pigments (Papers III and V).

Pigment	Trade name	shape	D_{50}, µm[1]	$(D_{75}- D_{25})/ D_{50}$ [2]	Shape factor[3]	Aspect ratio[4]	BET, m^2/g [6]
kaolin	Speswhite	flaky	0.60	2.50	20	16	13.2
kaolin	Kaovit	flaky	0.56	2.30	30	11	13.4
kaolin	Nuclay	flaky	0.48	2.08	36	~15 [5]	
kaolin	Amazon	flaky	0.20	0.92	4.6	8.2	18.4
kaolin	Kaofine	flaky	0.23	0.91	5.9		20.5
aragonite	Opacarb A40a	acicular	0.39	0.77	3.3	1.9	
aragonite	Opacarb A40b	acicular	0.39	0.77		4.6	
aragonite	Opacarb A60a	acicular	0.62	1.20	6.5	2.6	8.2
aragonite	Opacarb A60b	acicular	0.62	1.20		4.0	
aragonite	Opacarb mix	acicular	0.56	1.09	6.6	~3	8.8

1. Median equivalent spherical diameter measured by the Sedigraph (based on wt%).
2. An estimation of the width of the particle size distribution (based on wt%).
3. Mass-based median shape factor determined by the principal method.
4. Number-based median aspect ratio determined by image analysis.
5. Ojala (1976).
6. Specific surface area of the pigment measured by a nitrogen adsorption method.

4.2.3 Rheology

4.2.3.1 Intrinsic viscosity

The results of the fitting of measurements of plastic viscosity in the Bingham Eq. [68] against solids content to the Dougherty-Krieger Eq. [75] are shown in *Table 6*.

Table 6. Results from the rheological measurements using the Dougherty-Krieger Eq. [75] (Paper II)

Trade name	$[\eta]$	ϕ_m	$[\eta]\phi_m$
Speswhite	4.9	0.47	2.30
Kaofine	3.7	0.56	2.07
Kaovit	3.9	0.51	1.99
Amazon	3.7	0.59	2.18
Finntalc C10	4.6	0.46	2.12
Opacarb A40a	4.3	0.58	2.49
Opacarb A60a	4.3	0.54	2.32
Opacarb A80	4.9	0.52	2.55

For Speswhite, $[\eta]$ values of 5.0 (Rigdahl, Engström 1999) and 4.7 (Järnström, Rigdahl 1993) have been determined previously. Further, the product, $\eta\phi_m$, ranged from 1.60 to 2.55, and was therefore quite close to the assumption by Eiler (1941) that this product is 2.

The value of ϕ_m is affected by both the particle aspect ratio and the particle size distribution. A high value of ϕ_m is favoured by a low aspect ratio (and shape factor) and a broad particle size distribution. In table 6 it can be seen that Kaovit can be prepared to a higher solids content than Speswhite, although the particle size and particle size distributions of these pigments were about the same according to table 5. Apparently, the lower aspect ratio (by number) of the Kaovit particles was important. It can also be seen in table 6 that, considering their aspect ratios, the intrinsic viscosities of the acicular particles were rather high in comparison to the flaky particles, which can perhaps be expected from fig. 6. Moreover, table 6 shows that the intrinsic viscosity of the English clay, Speswhite, was 4.9, and that the intrinsic viscosities of the American clays, Kaofine and Kaovit, were approximately the same, slightly below 4. The fact that English and American clays have different origins and different production processes affects the surface chemistry of these clays. It is also conspicuous that $[\eta]$ for talc was only 4.6, although a number-based aspect ratio of 30 is reported by the manufacturer. This is certainly due to the complicated rheological behaviour of talc. It is hydrophobic and exhibited a pronounced dilatancy already at a low shear rate of 150 s^{-1}. Kaovit also exhibited a pronounced dilatancy, due to the high shape factor. The dilatancy of these pigments resulted in an uncertain determination of $[\eta]$, because only a small range of the flow curve can be used to fit the Bingham model, and thus to determine the viscosity of these suspensions.

It is clear from this investigation that the intrinsic viscosity in the Dougherty-Krieger Eq. [75] cannot be used directly as an estimate of the aspect ratio, but that additional information is needed. Nevertheless, some information about the aspect ratio is included in the intrinsic viscosity concept.

4.2.3.2 Capillary viscometry

Fig. 13 shows the viscosity plotted against shear rate for some pigment-only suspensions at 36.6 % solids content by volume. At low shear rates, the viscosity of the Speswhite suspension was much higher than those of the other pigment suspensions, which all had approximately the same viscosity. The fine fraction in the Kaovit must have had a large influence on the viscosity level. In all the pigment suspensions, dilatancy occurred already at a shear rate below 1000 s^{-1}. At high shear rates, all the suspensions except that containing Speswhite were clearly shear-thickening. The viscosities of Speswhite and Kaovit suspensions were about the same at 10^6 s^{-1}, although the difference was large at 10^5 s^{-1}, indicating an increasing importance of the shape factor with increasing shear rate for Kaovit. The performances of Kaofine and Amazon suspensions were very similar, although Kaofine ended up at a slightly higher viscosity, again owing to the higher shape factor. Opacarb A60a suspensions showed a more pronounced dilatancy than Opacarb mix suspensions.
The fine fraction in Opacarb mix (i.e. the Opacarb A40a component) obviously had a large influence. It is also noteworthy that the acicular particle suspensions had the highest viscosities at 10^6 s^{-1}, although the shape factors of these pigments were much lower than the shape factor for instance of Speswhite. It can be concluded that flaky particles in general performed much better at high shear rates than acicular particles, and thus orientated more easily in the flow field.

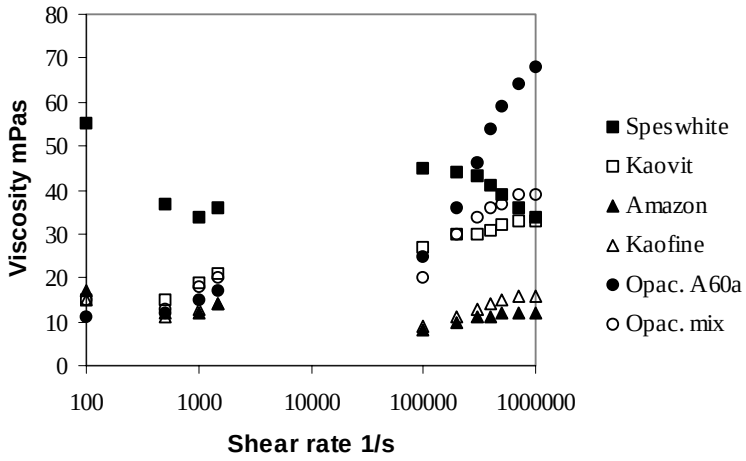

Fig. 13. Viscosity against shear rate for pigment-only suspensions at 36.6 % solids content, by volume (Paper III).

In the case of coating colours containing 10 pph latex and 1.0 pph CMC FF5 the performance was different from that of the pigment-only suspensions, see *Fig. 14.* At low shear rates, all the coating colours were shear-thinning and had much higher viscosity levels than the corresponding pigment-only suspensions. Speswhite colours had the highest viscosity, and the viscosities of the other colours were about the same. Even at high shear rates, the clay-based colours were mainly shear-thinning, whereas the aragonite colours were shear-thickening. The structure of a coating colour is to a large extent the result of interactions between pigment, latex and CMC, and this determines the properties of the colour at low shear rates, although at high shear rates the structure is mainly broken down. However, the possibility of a shear-

induced aggregation cannot be ignored (Gane et al. 1992). The viscosity of a pure CMC-solution at a concentration corresponding to that in the liquid phase of a coating colour (assuming no adsorption on pigment particles) is about 3 mPas at low shear rates (paper I). CMC-solutions are also known to be shear-thinning. At high shear rates, the shear viscosities of the coating colours and of the pigment-only suspensions should therefore be roughly comparable. The major differences are in the presence of latex spheres in the coating colour and in the solids content. The presence of spheres with a particle size of 0.15 µm tends to give a lower viscosity but, on the other hand, the solids volume fraction was higher in the coating colours (40.0 %) than in the pigment-only suspensions (36.6%).

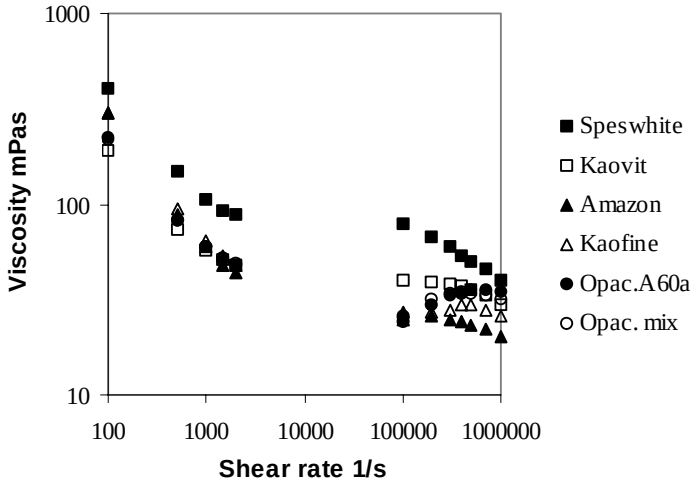

Fig. 14. Viscosity against shear rate for coating colours containing 10 pph latex and 1.0 pph CMC FF5 at 40.0 % solids content, by volume (Paper III).

Fig. 15 (*top*) shows the viscosities of the pigment-only suspensions and of the coating colours at 10^5 s^{-1}. The viscosities of the clay-based colours were much higher than those of the corresponding pigment-only suspensions. In the case of aragonite pigments, on the other hand, the values differed only slightly.

At 10^6 s^{-1} (*Fig. 15, bottom*), the viscosities of the Speswhite and Kaovit coating colours differed very little from those of the corresponding pigment-only suspensions. The added latex fraction had a lubricating effect that counteracted the increase in volume solids content. In the case of Amazon and Kaofine colours, on the other hand, the relative lubricating effect was smaller, since the shape factors of these pigments were low. Hence, the increase in solids content from pigment-only suspension to coating colour increased the viscosity level. In Opacarb A60a, the lubricating effect was pronounced due to the narrow shape factor distribution of this pigment and to the fact that it is difficult for needle-shaped particles to orientate in a shear flow even at rather low values of the shape factor. The difference between pigment-only suspension and coating colour in the case of Opacarb mix was much smaller, but the viscosity was lower for the coating colour.

It is clear that the presence of 10 pph latex sometimes had a pronounced lubricating effect, especially at a shear rate of 10^6 s^{-1}, which is of the same order as the shear rate under the blade during blade coating (assuming laminar flow). The lubricating effect was greatest when the

shape factor of the pigment was high and the shape factor distribution was narrow. In the sense relevant in this work, a “high” shape factor for flaky particles was about 20-30, whereas for acicular particles it was as low as 6-7. It is also possible to draw some conclusions about the viscosity at high shear rates from the composition of the coating colour.

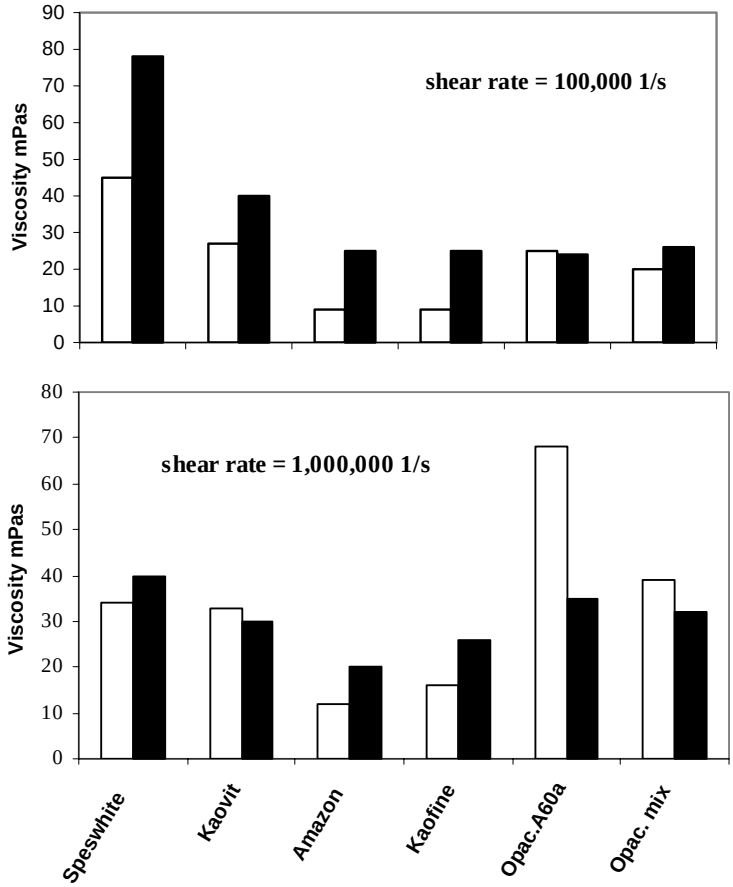

Fig. 15. Viscosities of pigment-only suspensions (unfilled bars) and coating colours (filled bars) at 100,000 s^{-1} (top) and 1,000,000 s^{-1} (bottom) (Paper III).

It is conspicuous that the viscosity of the Speswhite suspension (or colour) was higher than that of the suspension (or colour) based on Kaovit up to at least 10^6 s^{-1}, despite the high shape factor of the latter pigment. The influence of the fine fraction in Kaovit was therefore significant. For another delaminated clay, Nuclay, with a median shape factor of 36 and a rather broad particle size distribution (table 5), the viscosity was higher at different solids contents (58-64 %, by weight) than that of the corresponding Speswhite colours, see *Fig. 16.* It should be pointed out that the amounts of added CMC differed so that a Brookfield viscosity of 1 Pas was obtained for each colour. The amount of CMC added at a given solids content was always higher in the case of the delaminated clay. The higher viscosity of this delaminated clay (Nuclay) may be an effect mainly of the higher shape factor (36) compared to the other delaminated clay, Kaovit, with a median shape factor of 30.

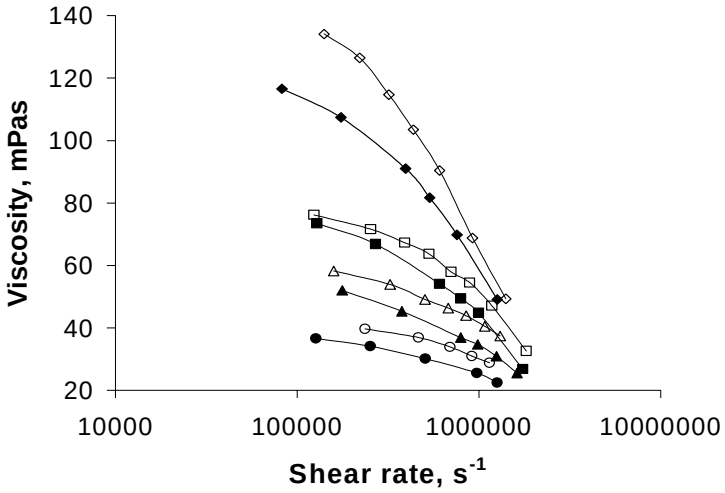

Fig. 16. Apparent viscosities for colours based on Speswhite (filled symbols) and Nuclay (open symbols) at solids contents of, from top to bottom, 64, 62, 60 and 58 %. The coating colours contained 10 pph latex and different amounts of CMC (Paper VI).

It was also shown that the overall runnability in a pilot plant was superior for colours based on Speswhite than for colours based on Nuclay, due to the very high shape factor and the poorer water retention ability of the latter pigment. This resulted in the appearance of streaks and stalagmite formation at lower machine speeds than what was the case with colours based on the English clay, which is in agreement with reports in the literature, where the overall better runnability of English clays than of delaminated clays was pointed out (Gane et al. 1992).

4.2.3.3 Entrance pressure losses and the slit die

Entrance pressure losses (EPL) are due mainly to elongational viscosity and possibly to elasticity. The packing ability of the particles must therefore have an effect, especially in the former case. The results obtained in different papers in this work are however apparently contradictory. In paper III, clay coating colours yielded significant non-Newtonian EPL in capillary viscometry, whereas this was not the case generally in the results reported in paper V. In paper VI, the non-Newtonian EPL were pronounced only at a high solids content (64 %, by weight). The same applies to colours based on aragonites. In paper III, no non-Newtonian EPL were found, in contrast to the results obtained in paper V. It should however be emphasised that the coating colour preparation procedure has been different in the different papers as well as the added amounts of water-soluble polymers, and that the aragonite pigments used were not the same in papers III and V, despite their similar trade names.

The conclusions that can be drawn are that non-Newtonian EPL increase with decreasing diameter of a capillary (or slit gap), and that non-Newtonian EPL seem to be dependent not only on the coating colour formulation, but also on the preparation procedure, for instance on the order of addition of the different components. Since non-Newtonian EPL may or may not be present in capillary viscometry, it is advisable to use more than one capillary for the measurements. *Fig. 17* shows for a coating colour based on one aragonite grade (Opacarb A40b) that the viscosity curves obtained with capillaries of similar diameter but different lengths do not coincide, and the Bagley correction has to be applied to obtain the shear viscosity of the sample. The apparent viscosity measured by any one of the capillaries was overestimated by at least 100 %. Fig. 17 also shows that the non-Newtonian EPL in a slit die were significant, and this was the case for all of the coating colours based on different pigments. It should be emphasised that the aragonite grade (Opacarb A40b) in Fig. 17 had quite a high aspect ratio (4.6) (table 5).

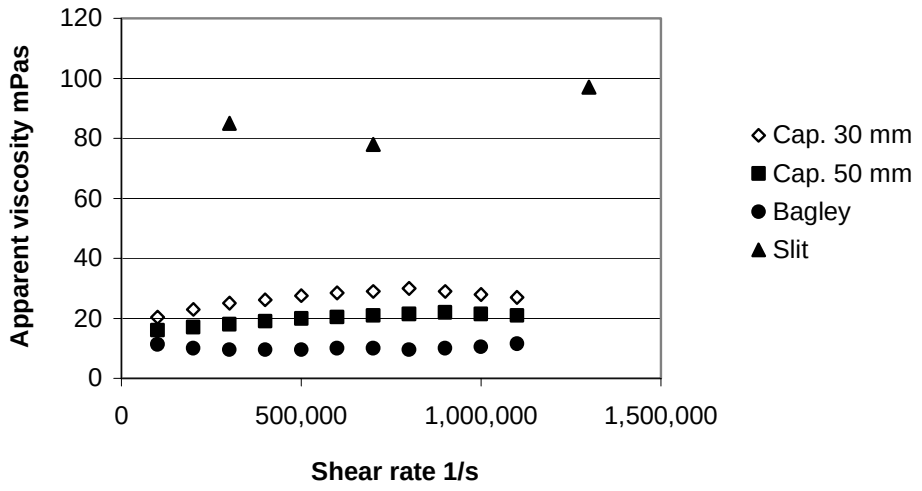

Fig. 17. Apparent viscosity curves obtained by capillaries and a slit die, as well as the Bagley corrected curve, for a coating colour based on aragonite, Opacarb A40b, with no CMC, 10 pph latex and a solids content of 58 %, by weight (Paper V).

Fig. 18 shows the relative contributions to the total pressure drop required to attain a shear rate of 1,000,000 s^{-1} in a capillary with a diameter of 50 mm. The average value for all colours containing a particular pigment is given, since the dependence on the solids content and on the presence of polymers was small. The three contributions taken into account were shear viscosity within the capillary, Newtonian EPL predicted by the kinetic energy correction (Eq. [76]), and non-Newtonian EPL (the Bagley correction and Eq. [77]). Pressure losses at the exit of the capillary were considered to be negligible. The shear viscosity was in general the predominating contribution to the overall pressure drop, except in the case of the Opacarb A40b colours. In that case, the EPL predominated clearly over losses due to shear viscosity, possibly owing to the rather high aspect ratio of the aragonite particles, which meant that it was difficult for these particles to orientate in the flow field during the acceleration at the entrance of the capillary. The difference in aspect ratio between the Opacarb A40b and Opacarb A60b pigments may seem small in table 5, but it is possible that there is some intermediate threshold above which a more complicated flow behaviour develops.

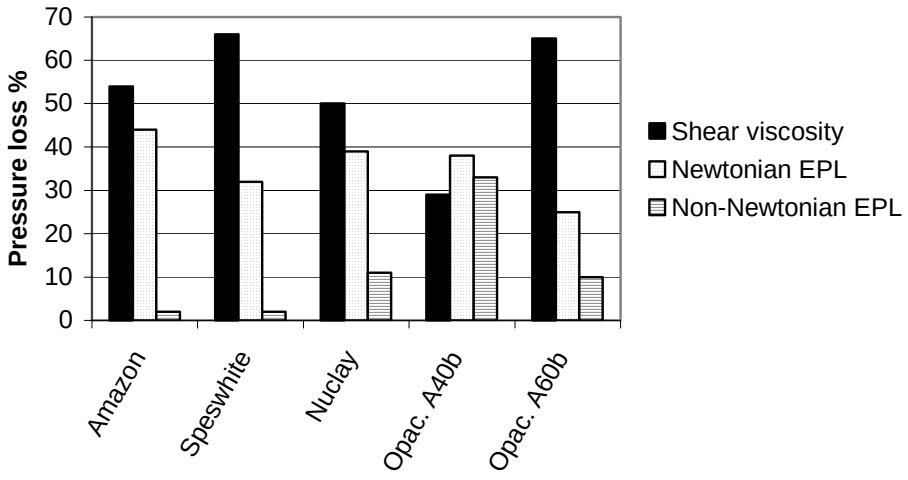

Fig. 18. Relative contributions to the pressure loss at a shear rate of 1,000,000 s^{-1} in capillary viscometry (capillary diameter of 50 mm). Average values for all colours containing a particular pigment (Paper V).

The non-Newtonian EPL amounted to at least 10 % of the total pressure drop for colours based on Nuclay, Opacarb A40b and Opacarb A60b, indicating for instance that the shear viscosities of these colours cannot be properly estimated using only one capillary, in contrast to colours based on Amazon and Speswhite.

Fig. 19 shows similar relative contributions to the total pressure drop at the same shear rate using a slit die. Complete series (six colours) could only be measured in the cases of the colours based on Speswhite and Opacarb A60b. For series of colours containing the other pigments, measurements were not performed on more than three colours in any one case. The Newtonian EPL were calculated according to Eq. [82], and the non-Newtonian EPL were calculated using Eqs. [83]-[85] and [87], where the shear viscosity obtained by capillary viscometry has been applied. This is based on the assumption that a Newtonian fluid would

give the same apparent viscosity (i.e. the shear viscosity) regardless of whether a capillary or a slit die were used. Again, the average values for all colours based on a given pigment have been calculated, but the values were more influenced by the solids content, and particularly by the presence of polymers, than the results obtained using capillaries. Nevertheless, the overall trend in fig. 19 is clear. The contribution of the shear viscosity to the total pressure drop did not exceed 40 % in any single case. The non-Newtonian EPL were always significant, especially in the case of aragonite-based colours.

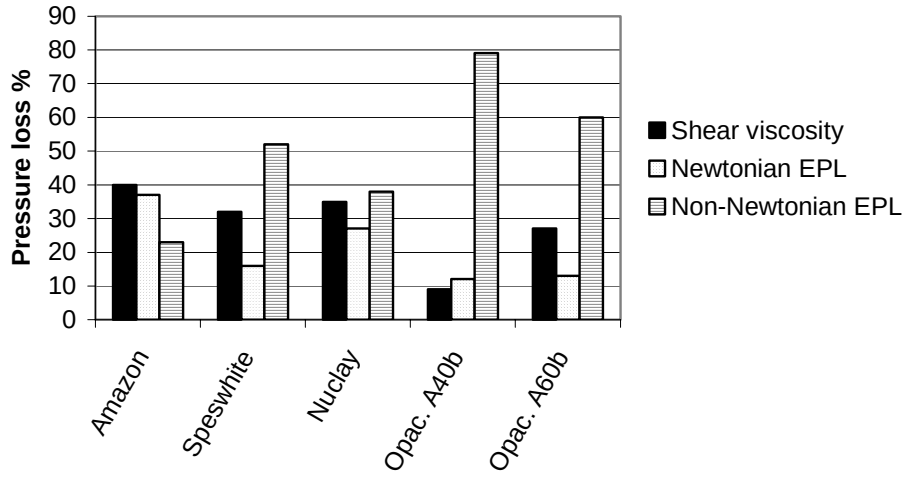

Fig. 19. Relative contributions to the overall pressure loss using a slit die at a shear rate of 1,000,000 s^{-1}. Average values for all colours containing a particular pigment (Paper V).

Fig. 20 shows for the colours without water-soluble polymers the ratio between the apparent viscosity measured with the slit die and the corresponding shear viscosity, which is an indication of the influence of the relative non-Newtonian EPL on the performance for each type of pigment. The ratio was about 2 for colours based on clay pigments (slightly increasing with increasing shape factor of the pigment), but it was much higher for aragonite-based colours, especially in the case of colours based on Opacarb A40b. This was again probably due to the higher aspect ratio of these particles compared to that of the Opacarb A60b particles (table 5), which means that it was extremely difficult for the particles to align in the flow direction during the acceleration at the slit entrance. High shape factors of flaky particles, above 30, apparently give rise to rather small non-Newtonian effects at the entrance of the slit, whereas needle-shaped particles yield pronounced effects already at very low aspect ratios, below 5. The anisotropic character of the pigment seemed to play a significant role, see fig 3.

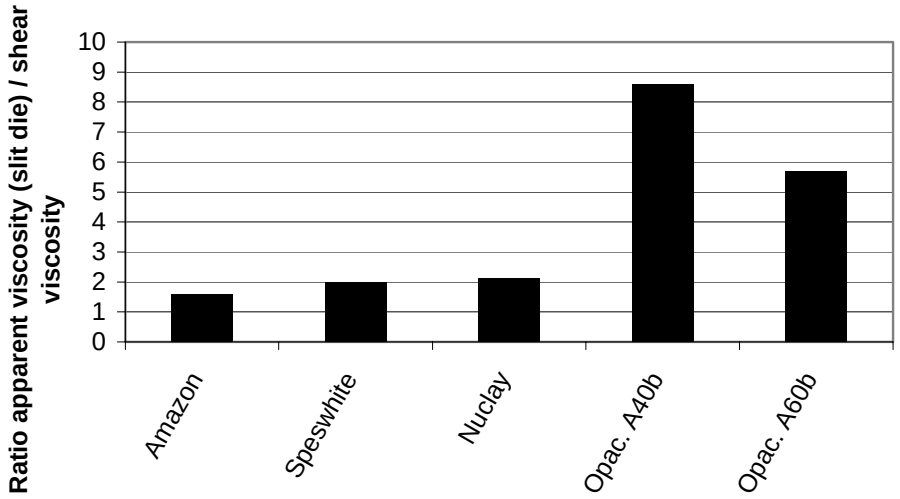

Fig. 20. Influence of the type of pigment on the relative non-Newtonian EPL in a slit die at a shear rate of 1,000,000 s^{-1} for colours containing 10 pph latex but no water-soluble polymer. Average values for different solids contents (Paper V).

4.2.4 Properties of coating layers

4.2.4.1 Coatings on aluminium foil

Fig. 21 shows the porosities, i.e. percentage void volumes, for coating layers on aluminium foil prepared from pigment-only suspensions, from pigment suspensions to which 1.0 pph CMC FF5 has been added, and from suspensions where both 1.0 pph CMC FF5 and 10 pph latex had been added (i.e. ”complete” coating colours).

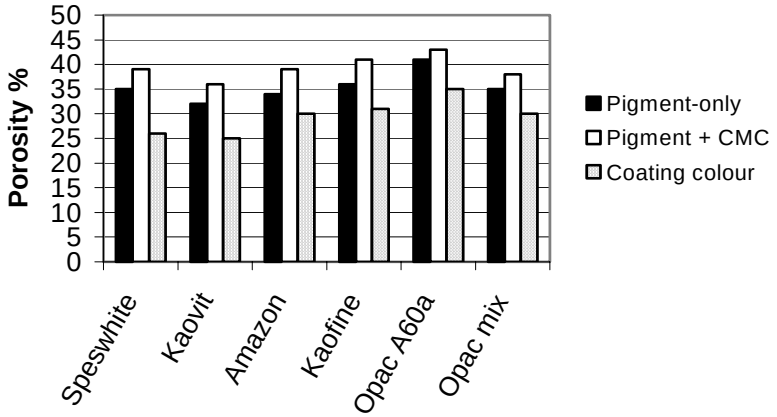

Fig. 21. Porosities of coating layers on aluminium foil. For each pigment, coating layers were prepared from a pigment-only suspension, a suspension containing pigment plus 1.0 pph CMC FF5 and a suspension containing pigment, 1.0 pph CMC FF5 and 10 pph latex (coating colour). 60 % solids content, by weight (Paper IV).

As can be seen in fig. 21, the trend was the same for each pigment; the porosity was greater when CMC was added than in pigment-only layers, presumably due to aggregation, but it was significantly lower when latex was also present. A broader shape factor distribution (cf. Speswhite and Kaovit; Opacarb A60a and Opacarb mix) resulted in a tighter packing and a lower porosity in all cases. However, no blends of pigments have been used in this work. Hagemeyer (1960) found that blends of 20 % rhombic (or aragonitic) PCC and 80 % clay resulted in a reduced packing ability compared with that of pure clay systems. A blend of rhombic PCC and clay, compared to the pure clay, can in a sense be regarded as an increase in the shape factor distribution. The decrease in porosity in the presence of latex was more pronounced for coarse clays than for fine clays. The porosities of Kaofine-based layers were slightly higher than those of Amazon-based, indicating a slightly tighter packing in the latter case. One reason for this may be the higher shape factor at the coarse end of the size distribution for Kaofine (fig. 12). However, the pigment particle size and shape are not the only factors affecting the porosity. Colloidal interactions can also have an influence (Lepoutre, Lord 1990), and such interactions may be different for pigments of different origins.

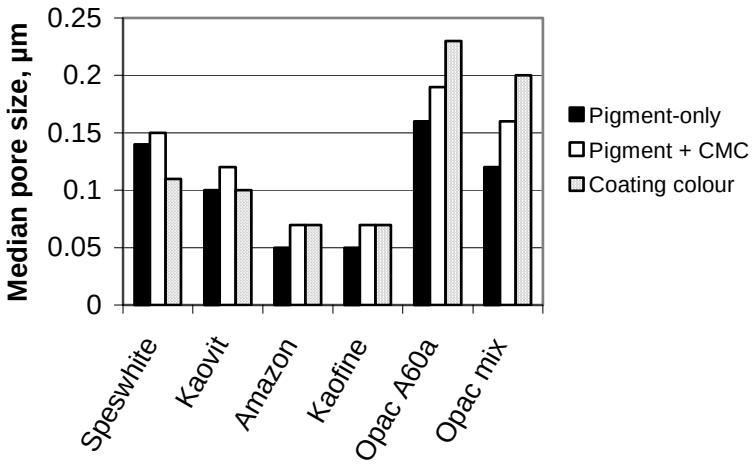

Fig. 22. Median pore sizes for the same coating layers as in fig. 21 (Paper IV).

The average pore sizes of the coating layers obtained by mercury porosimetry are shown in *Fig. 22*. It is mainly the relative pore sizes of different layers that are interesting, so that a ranking of the samples is assumed to be possible. It is clear that the median pore size decreased with increasing width of the shape factor distribution (cf. Speswhite and Kaovit; Opacarb A60a and Opacarb mix). In the case of the aragonite pigments, the average pore size was apparently larger in the layer based on coating colours than in the layers containing only pigment and CMC. This was presumably due to the low specific surface area (see table 5), which means that the small pores were more or less filled with latex during drying. The average pore size thus shifted towards larger values in the presence of latex, at the same time as the porosity decreased (fig. 21). It may also be so that the pore-to-throat size ratio changes in the presence of latex during drying, so that the size of the neck of the pore will increase

relative to the pore size. Nevertheless, the pore size was in general larger for aragonite-based than for clay-based layers.

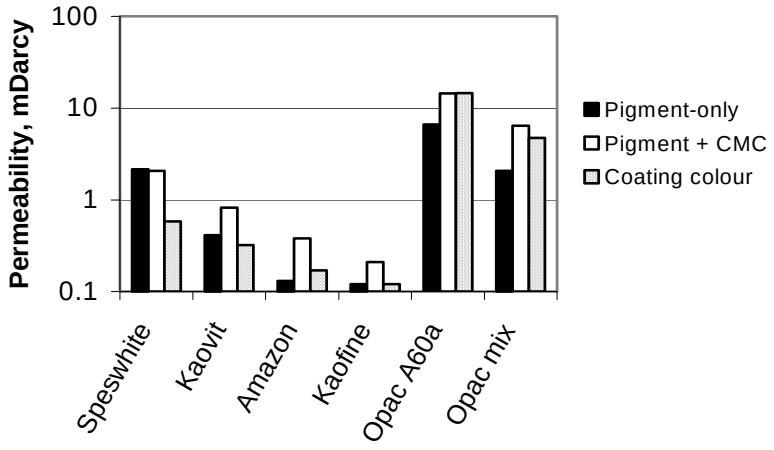

Fig. 23. Darcian liquid permeabilities, calculated by a computer algorithm (Pore-Cor), for the same coating layers as in fig. 21 (Paper IV)

Fig. 23 shows the results of using a computer algorithm (Pore-Cor) to calculate the Darcian liquid permeabilities of the coating layers. The permeabilities of Kaofine-based layers were here found to be lower than those of Amazon-based layers, even though the porosities were higher in the latter case and the average pore sizes were about the same for both types of layer. Nevertheless, in general, a higher porosity and a larger median pore size meant a higher permeability. The permeabilities of the pigment-only layers and of the coating colour layers correlated quite well with in average pore sizes (fig. 22) as well as with in viscosities of the corresponding pigment-only suspensions and colours at high shear rates (10^6 s^{-1}), see fig. 15. Hence, a broader shape factor distribution also resulted in a lower permeability (fig. 23).

4.2.4.2 CLC Coatings on paper

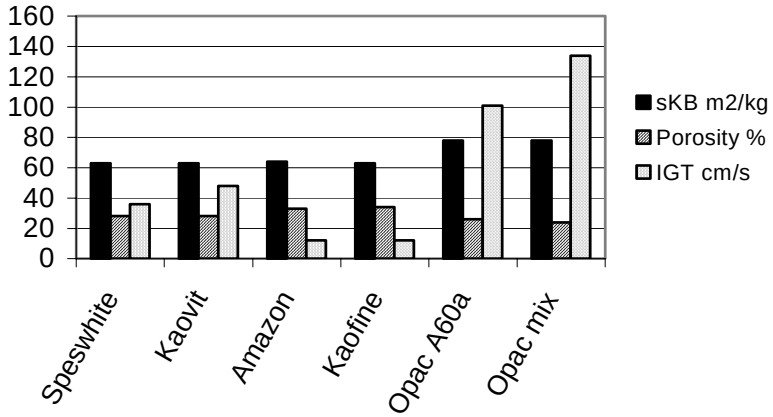

Fig. 24. Light scattering coefficient, porosity and IGT pick resistance of coated papers. All colours contained 1.0 pph CMC FF5 and 10 pph latex. Solids content, clay-based colours: 60 %; aragonite-based colours 62 % (by weight). Approximate coat weight 10 g/m^2,
s_{KB} value of the base paper 72 m^2/kg (Paper IV).

Fig. 24 shows the Kubelka-Munk light scattering coefficient (see Bristow, Kolseth 1986), s_{KB}, at an effective wavelength of 457 nm, the porosity and the IGT pick resistance for coating layers on paper. The data were interpolated to correspond to a coat weight of 10 g/m^2. These three properties all depend on the packing of the pigment particles and can therefore be expected to be related to one another. s_{KB} was approximately the same for all the clay-based coating layers, even though the porosities of the layers prepared from fine clays were higher than those prepared from coarse clays. The lower porosity of the coarse clay layers was apparently counteracted by a larger average pore size that scatters light more efficiently. It should however be pointed out that the measured s_{KB} was the result of a combined scattering from both the coating layer and the base paper beneath, including a complex interaction between the two layers. The influence of the base paper on the coating layer cannot be considered to be the same for different coatings, since the water retention ability differs for different systems and the amount of latex that penetrates the paper, mainly in the liquid phase of the coating colour, will also differ.

If the pigments with a broad shape factor distribution are compared with those with a narrow distribution, i.e. if Speswhite is compared with Kaovit and Opacarb A60a with Opacarb mix, no difference can be seen in s_{KB} and the porosity was only slightly lower for Kaovit and Opacarb mix. The difference in IGT pick resistance was however significant, especially whenOpacarb A60a is compared to Opacarb mix. A high pick resistance is favoured by a low porosity and large pores, i.e. a small free particle surface area. The adhesion of latex to the pigment particles is also important. The pores in the coating layers based on Opacarb A60a seem to be too large to scatter light efficiently compared to layers based on Opacarb mix. Further, needle-shaped particles scattered light more efficiently than flaky particles. In this work, this was probably due to a larger average pore size that is closer to the optimum size with regard to light scattering. It may also be that the majority of the pores in the sample belong to particular shape groups, which are different for flaky and for acicular particles. In this case, the characteristic shape of the pores in an aragonite-based structure may scatter light more efficiently. The optimum pore size for this purpose for clay structures, taken as the minor dimension of an oblate spheroid, has been shown to be 0.5 – 0.7 µm, when the aspect ratio of the spheroid was varied between 1.6 and 2.2 (Climpson, Taylor 1976). This value cannot of course be directly compared to the mercury porosimetry data, since this method clearly underestimates the median pore size.

Opacarb mix seems to be a good pigment choice if both high light scattering and high mechanical strength are required. The viscosity at high shear rates of a coating colour prepared from Opacarb mix was also lower than that of a colour based on Opacarb A60a (fig. 15).

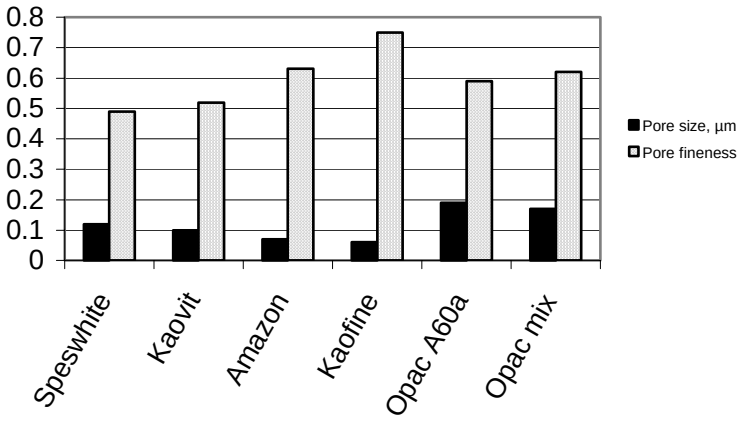

Fig. 25. Median pore sizes for the same coatings as in fig. 24. A pore fineness parameter, determined from reflectance measurements, is also given (Paper IV).

Fig. 25 shows the median pore size determined by mercury porosimetry for the coating layers on paper. A pore fineness parameter, ϖ, is also given. This is derived from the relation between s_{KB} and the wavelength of the incident light, λ (Gate 1972):

$$s_{KB} = c\lambda^{-\varpi} \qquad [89]$$

where c is a constant. The parameter ϖ is a measure of the mean hydraulic diameter of the pores in the coating layer. ϖ is given by the slope of the linear relation when s_{KB} is plotted versus λ in a log-log diagram. According to this empirical relationship, a large value of ϖ corresponds to a small pore diameter and vice versa. ϖ can therefore be interpreted as being a measure of the pore fineness.

The empirical Eq. [89] is supported by the results shown in fig. 25, as long as a given particle shape, flaky or acicular, is concerned. However, comparisons can obviously not be made between these two particle shapes since, compared to the clay-based layers, the large pores given by mercury porosimetry for the aragonite-based layers were associated with too large values of ϖ. In the case of clay pigments, the pore sizes of coating layers on paper were about the same as those of the corresponding coating layers on aluminium foil, whereas the pores were smaller in coatings on paper in the case of the aragonite-based layers. This was in agreement with the fact that the porosities of aragonite-based coatings on paper were lower than those on aluminium foil, but some latex may have penetrated into the paper beneath the coating in the former case, which means that less latex remained to fill and block the small pores, and the median pore size in the coating was then shifted towards smaller values. The difference in pigment particle packing ability between aragonite-based layers on an aluminium substrate and on paper would then have been even larger than indicated by the measurements.

5. Concluding remarks

- For suspensions containing monodisperse spherical polystyrene particles, a concentration gradient appeared in the filter cake forming during filtration under static conditions. Such a gradient, monitored by non-destructive magnetic resonance imaging (MRI), is not accounted for in traditional filtration theory used in coating technology. Good agreement was found between a literature model describing filtration with a compressible filter cake and the concentration gradients measured by MRI. This model showed that the scaled concentration gradient was the same at all times.

- A rapid method to estimate a shape factor of flaky and acicular pigment particles has been evaluated. Generalised mathematical models of oblate and prolate spheroids are used, and the shape factor is derived from a comparison between the results obtained by two different size-determining instruments. This method yields a shape factor distribution as a function of equivalent spherical particle size, but the results are uncertain for small particles, < 0.2 µm. The shape factor can be regarded as a mass-based aspect ratio, but it is an engineering approach, and the results should be used for ranking the samples rather than as absolute values.

- The median shape factor was an important parameter for the high-shear viscosity, but information about the shape factor distribution was also important for an appropriate understanding, and such information is in part given by the rapid method mentioned above.

- Entrance pressure losses in capillary viscometry were sometimes in part non-Newtonian, indicating that it was inappropriate to measure the shear viscosity with only one capillary. Such effects were however much more pronounced in slit die viscometry, in a relative sense. They were roughly independent of the shape factor of kaolin particles, whereas the dependence on the aspect ratio of aragonite particles was significant.

- The shape factor was an important parameter for the pore structure of a coating layer, and for properties depending on the pore structure. The porosity of a coating layer based on fine kaolin clay with a low shape factor was in general higher than that of a coating based on coarse clay with a high shape factor, but the average pore size was considerably larger for the coarser pigment.

- The trend in high shear viscosity of coating suspensions based on different pigments followed the trend in median pore size of the corresponding coating layer, rather than the trend in porosity.

- A continuation of this work would be to improve the calculation of scattering coefficients in the principal method, by developing and using algorithms for spheroids rather than for a sphere. This would improve the precision in the calculation of the shape factor, and probably reduce the need for a rather arbitrary empirical correction, such as the one used in this work.

Acknowledgements

First and foremost I would like to express my gratitude to my supervisor Mikael Rigdahl for his extraordinary competence and for always supporting me in all situations throughout this work. I would also like to thank my examiner Bo Norman for his support. My coauthors are acknowledged, and Tomas Larsson is thanked for writing the computer algorithms in appendices 1 and 2.

I am indebted to the Surface Treatment group at the Swedish Pulp and Paper Research Institute (STFI), in particular to Lucyna Lason and Jolanta Borg for skilled experimental assistance. Other groups at STFI, who have directly or indirectly contributed to this work, are also acknowledged. Anthony Bristow and Ingrid Fineman are thanked for many valuable comments on the manuscripts, the former also for the linguistic revisions.

The Swedish Mineral Processing Research Association (MinFo), the Swedish National Board for Industrial and Technical Development and the Swedish Research Council for Engineering Science (TFR) are thanked for financial support for some of the projects included in this thesis.

References

Aitchison, J and Brown, J A C (1969)
"The Log-normal Distribution"
University Press, Cambridge, England

Allen, T (1981)
"Particle Size Measurement"
Chapman and Hall Ltd, London, England

Bagley, E B (1957)
End corrections in the capillary flow of polyethylene
J. Appl. Phys. **28**:624

Barnes, H A, Hutton, J F and Walters, K (1989)
"An Introduction to Rheology"
Elsevier, Amsterdam, Netherlands

Baudet, G, Bizi, M and Rona, J P (1993)
Estimation of the average aspect ratio of lamellae-shaped particles by laser diffractometry.
Particulate Sci. Technol., **11**, 73-96

Binding, D (1998)
Personal communication

Bohren, C F and Huffman, D R (1983)
"Absorption and Scattering of Light by Small Particles"
John Wiley & Sons, New York, USA

Bristow, J A and Kolseth P (1986)
In "Paper Structure and Properties"
Marcel Dekker Inc., New York, USA

Cadle, R D (1965)
"Particle Size"
Reinhold Publishing Corporation, Chapman & Hall Ltd, London, England

Carreau, P J, De Kee, D C R. and Chhabra, R P (1997)
"Rheology of Polymeric Systems"
Carl Hanser Verlag, Munich, Germany

Climpson N A and Taylor J H (1976)
Pore size distribution and optical scattering coefficients of clay structures
Tappi **59**(7):89

Coulson J M and Richardson J F (1978)
"Chemical Engineering" vol. 2
Pergamon Press, Oxford, England

Cumberland D J and Crawford R J (1987)

"The Packing of Particles" vol. 6
Elsevier, Amsterdam, Netherlands

Daicic, J and Furó, I (1999)
NMR cryoporometry: A novel method for the investigation of the pore structure of paper and paper coatings
Nordic Pulp Pap. Res. J. **14**(3), 221

Engström, G (1986)
Development of the solids content in the coating layer between application and blade
Wochbl. Papierfabr. **114**:6, 195

Engström, G and Rigdahl, M (1992)
The use of some PCC grades as coating pigments
Nord. Pulp Pap. Res. J. **7**(2):90

Eiler, H (1941)
Die Viskosität von Emulsionen hochviskoser Stoffe als Funktion der Konzentration
Colloid Z. Z. Polymer **97**, 313

Eriksson, U and Rigdahl, M (1994)
Dewatering of coating colours containing CMC or starch
J. Pulp Paper Sci. **20**:11, J333.

Einstein, A (1906)
Eine neue Bestimmung der Moleküldimensionen
Ann. Physik **19**, 289

Frisch, H L and Simha, R (1956)
The viscosity of colloidal suspensions and macromolecular solutions
Rheology **1**, 525

Gane, P A C, Kettle, J P, Matthews, P G and Ridgway, C J (1996)
Void space structure of compressible polymer spheres and consolidated calcium carbonate paper coating formulations
Ind. Eng. Chem. Res. **35**, 1753

Gane, P A C, McGenity, P M and Watters, P (1992)
Factors influencing the runnability of coating colours at high speed
Tappi J. 75:5, 61

Gane, P A C and Seyler, E N (1994)
Tack development: An analysis of ink/paper interaction in offset printing
Proc. Tappi Coating Conference, Tappi Press, Atlanta, 243

Gate, L (1972)
Light scattering in micro porous materials using photon diffusion model
Physics D: Appl. Physics **5**:837

Graton, L C and Fraser, H J (1935)
Systematic packing of spheres
J. Geology **43**:8, 785

Greenblatt, G and Wilson, T S (1995)
Capillary viscometry of paper coating colours and correlation to coat weight development in blade coating
Polym. Mater. Sci. Eng. **73**:484

Hagemeyer, R W (1960)
The effect of pigment combination and solids concentration on particle packing and coated paper characteristics
Tappi **43**(3):277

Hagemeyer, R W (1964)
The effect of particle shape and chemical composition on the packing characteristics of pigment combinations
Tappi **47**(2):74

Happel, J and Brenner, H (1965)
Low Reynolds Number Hydrodynamics
Prentice Hall, New Jersey, USA

Hwang, K-J, Wu, Y-S and Lu, W-M (1997)
Effect of the size distribution of spheroidal particles on the surface structure of a filter cake
Powder Technol. **91**, 105

Jefferey, G B (1923)
The motion of ellipsoidal particles immersed in a viscous fluid
Proc. Roy. Soc., London A102, 161

Jennings, B R and Parslow, K (1988)
Particle size measurement: the equivalent spherical diameter
Proc. Roy. Soc., London A419, 137

Järnström, L and Rigdahl, M (1993)
Aggregation in coating colours based on mixtures of kaolin and aluminia trihydrate
Nord. Pulp Pap. Res. J. **8**(2), 273

Kettle, J P and Matthews, G P (1993)
Computer modelling of the pore structure and permeability of pigmented coatings
Tappi Adv. Coating Fund. Symp., Tappi Press, Atlanta, USA, 121

Konakawa, Y and Ishizaki, K (1990)
The particle size distribution for the highest relative density in a compacted body
Powder Technol. **63**, 241

Krieger, I M (1972)
Rheology of monodisperse latices
Adv. Coll. Interf. Surf. **3**, 111

Krieger, I M and Dougherty, T J (1959)
A mechanism for non-Newtonian flow in suspensions of rigid spheres
Trans. Soc. Rheology **3**, 137

Kuhn, W and Kuhn, H (1945)
Die Abhängigkeit der Viskosität vom Strömungsgefälle bei hochverdünnten Suspensionen und Lösungen
Helv. Chim. Acta **28**, 97

Landman, K A, Sirakoff, C and White, L R (1991)
Dewatering of flocculated Dispersions by Pressure Filtration
Phys. Fluids A. **3**:6, 1495

Lepoutre, P and Lord, D (1990)
Destabilised clay suspensions: flow curves and dry film properties
J. Colloid Interf. Sci. **134**:66

Letzelter, P (1997)
Dewatering of coating colours: a filtration or thickening mechanism
Tappi Adv. Coating Fund. Symp., Tappi Press, Atlanta, USA, 103

Lindhjem, C E (1991)
Particle packing and shape effects on the rheological characteristics of paper coating pigments
Proc. Tappi Coating Conf., Tappi Press, Atlanta, USA, 131

Mäkinen, M (1999)
Personal contact

Matthews, G P, Ridgway, C J and Spearing, M C (1995)
Void space modeling of mercury intrusion hysteresis in sandstone, paper coating, and other porous media
J. Colloid Interf. Sci. **171**, 8

Morris, H H, Sennett, P, and Drexel, R J (1965)
Delaminated clays - physical properties and paper coating properties
Tappi **48**(12), 92A

Ojala V M (1976)
Undersökningar av partikelform för bestrykningspigment (in Swedish)
Master thesis work performed at Åbo Akademi, Finland

Olsson, F and Isaksson, P (1995)
The influence of viscoelastic rheology on blade coating as revealed by numerical methods
Nordic Pulp Pap. Res. J. **4**, 234

Powell, M J (1980)
Computer simulated random packing of spheres
Powder Technol. **25**, 45

Reyes, S C and Iglesia, E (1991)
Monte-Carlo simulations of structural properties of packed beds
Chem. Eng. Sci **46**(4), 1089

Rigdahl, M and Engström, G (1999)
Personal communication

Scarlett, B (1997)
Personal communication

Simha, R (1940)
The influence of brownian movement on the viscosity of solutions
J. Phys. Chem. **44**, 25

Slepetys, R A and Cleland, A J (1993)
Determination of shape of kaolin pigment particles
Clay Minerals **28**, 495

Soppe, W (1990)
Computer simulation of random packings of hard spheres
Powder Technol. **62**, 189

Sullivan, T and Middleman, S (1986)
Film thickness in blade coating of viscous and viscoelastic fluids
J. Non-Newtonian Fluid Mech. **21**, 13

Suzuki, M and Oshima, T (1985)
Coordination number of a multi component randomly packed bed of spheres with size distribution
Powder Technol. **44**, 213

Tiller, F M, Yeh, C S and Leu, W F (1987)
Compressibility of particulate structures in relation to thickening, filtration, and expression - a review
Sep. Sci. Techn. **22**, 2 and 3, 1037

Tsuji, A, Nitta, J, Sasagawa, Y and Nojima, N (1990)
A new rheometer for paper coating
Tappi J. **73**:9, 163

Whorlow, R W (1992)
"Rheological Techniques"
Ellis Horwood Ltd, Chichester, England

Willenbacher, N and Hanciogullari, H (1997)
Analysis of Coating Colour Runnability Considering the Effect of Dewatering
Proc. Tappi Coating Conf., Tappi Press, Atlanta, USA, 1

Appendix 1

Calculation of r from Eq. [57] for an oblate spheroid

i.e. solution of the equation

$$\left(\frac{d_{sos}}{d_{lsos}}\right)\sqrt{\frac{s_{os}}{s_{sp}}} = \sqrt{\frac{2r\arctan\sqrt{(r^2-1)}}{r\sqrt{(r^2-1)}+\ln(r+\sqrt{(r^2-1)}}}$$

```
$declare
c
c     Arguments:
c     ds    : Stokes diameter
c     dls   : light scattering diameter
c     rpr   : real part of particle refractive index
c     rpi   : imag. part of particle ref. index
c     rm    : real part of medium ref. index
c     wl    : wavelength of laser light
c     ************************************
c     wl, ds and dls must have the same units (i.e. um)
c     ************************************
      double precision function lom(a_ds [value], a_dls [value],
     +    a_rpr [value], a_rpi [value], a_rm [value], a_wl [value])

      double precision a_ds,a_dls,a_rpr,a_rpi,a_rm,a_wl

      complex s1(20), s2(20), refrel
      real ds,dls,rpr,rpi,rm,wl
      real x,qext,qsca,qback, sos, ssp, sspold, dssp
      real rmax, rmin, r, dv, a
      integer iter
      real zero, rtbis
      external zero

      real tmp

      common /arg/ ds, dls, sos, ssp

      real C_PI, C_TOL
      integer C_MAXITER, C_NANG
      parameter(C_PI=3.1415926536,
     +          C_TOL=1.0e-4,
     +         C_MAXITER=100,
     +         C_NANG=3)

C     *******************************

      ds=a_ds
      dls=a_dls
      rpr=a_rpr
      rpi=a_rpi
      rm=a_rm
      wl=a_wl

      refrel=cmplx(rpr,rpi)/rm


      x=C_PI*dls*rm/wl
      call bhmie(x,refrel,C_NANG,s1,s2,qext,qsca,qback)
      sos=qsca
c     **********************
c     Start iteration for finding r
c     **********************
      ssp=sos
      iter=0
 10   continue

        sspold=ssp
```

```
      rmax=10.0
      rmin=1.0+epsilon(rmin)

 20    continue

      r=rtbis(zero,rmin,rmax,C_TOL)
c     ********************************************
c     If the root is not in the interval [rmin,rmax], increase rmax.
c     Note ! the upper limit is related to the maximum number of iterations
c     in rtbis
c     ********************************************
      if ((r.eq.-101.0).and.(rmax.le.1.0e16)) then
         rmax=rmax*10.0
         goto 20
      endif
c     *************************
c     Make sure that rtbis did not fail
c     *************************
      if (r.lt.0.0) then
         lom=r
         goto 999
      endif
      a=ds/sqrt(atan(sqrt(r*r-1.0))/sqrt(r*r-1.0))
      dv=a/(r**(1.0/3.0))

      x=C_PI*dv*rm/wl
      call bhmie(x,refrel,C_NANG,s1,s2,qext,qsca,qback)
      ssp=qsca

      iter=iter+1
      if (iter.gt.C_MAXITER) then
         lom=-1.0
         goto 999
      endif
c     *************************
c     rfunc(r) is bounded by ] 0, 1 [
c     *************************
      tmp=ds/dls*sqrt(sos/ssp)
      if (ds/dls*sqrt(sos/ssp).gt.1.0) then
         lom=-2.0
         goto 999
      endif

      dssp=abs((ssp-sspold)/ssp)
      if (dssp.le.C_TOL) then
         lom=r
         goto 999
      endif

    goto 10

 999  continue
c     write(6,*) 'Iter = ', iter
c     write(6,*) 'Zero =' , zero(r)
c     write(6,*) 'rmax =' , rmax
    end

C**********************************************************************
    real function rfunc(r)
    real r
```

```
      real f0,f1,f2,f3

       f0=sqrt(r*r-1.0)
       f1=2.0*r*atan(f0)
       f2=r*f0
       f3=log(r+f0)

       rfunc=sqrt(f1/(f2+f3))

      end
C**********************************************************************
c     double precision function rfunc2(r [value])
c     double precision r
c     double precision f0,f1,f2,f3

c     f0=sqrt(r*r-1.0)
c     f1=2.0*r*atan(f0)
c     f2=r*f0
c     f3=log(r+f0)

c     rfunc2=sqrt(f1/(f2+f3))

c     end
C**********************************************************************
      real function zero(r)
      real r, ds, dls, sos, ssp
      common /arg/ ds, dls, sos, ssp
      real rfunc
      real f1,f2,f3

      f1=rfunc(r)
      f2=(ds/dls)*sqrt(sos/ssp)
      f3=f1-f2
      zero=f3

      end
C**********************************************************************

      subroutine bhmie(x, refrel, nang, s1, s2, qext, qsca, qback)

      complex s1(20), s2(20)
      real x, qext, qsca, qback
      integer nang

      real amu(10), theta(10), pi(10), tau(10), pi0(10), pi1(10)
      complex d(3000), y, refrel, xi, xi0, xi1, an, bn
      double precision psi0, psi1, psi, dn, dx

      real xstop, ymod, dang, rn, chi0, chi1, apsi0, apsi1
      real fn, chi, apsi, p, t
      integer nstop, nmx, j, nn, n, jj

      real C_PI
      parameter(C_PI=3.1415926536)

C     ******************************

      dx=x
      y=x*refrel
```

```
      xstop=x+4.0*x**(1.0/3.0)+2.0
      nstop=xstop
      ymod=cabs(y)
      nmx=amax1(xstop,ymod)+15
      dang=C_PI/2.0/float(nang-1)

      do 555 j=1,nang
         theta(j)=(float(j)-1.0)*dang
         amu(j)=cos(theta(j))
  555 continue

      d(nmx)=cmplx(0.0,0.0)
      nn=nmx-1
      do 120 n=1,nn
         rn=nmx-n+1
         d(nmx-n)=(rn/y)-(1.0/(d(nmx-n+1)+rn/y))
  120 continue

      do 666 j=1,nang
         pi0(j)=0.0
         pi1(j)=1.0
  666 continue

      nn=2*nang-1
      do 777 j=1,nn
         s1(j)=cmplx(0.0,0.0)
         s2(j)=cmplx(0.0,0.0)
  777 continue

      psi0=dcos(dx)
      psi1=dsin(dx)
      chi0=-sin(x)
      chi1=cos(x)
      apsi0=psi0
      apsi1=psi1
      xi0=cmplx(apsi0,-chi0)
      xi1=cmplx(apsi1,-chi1)
      qsca=0.0
      n=1

  200 dn=n
      rn=n
      fn=(2.0*rn+1.0)/(rn*(rn+1.0))
      psi=(2.0*dn-1.0)*psi1/dx-psi0
      apsi=psi
      chi=(2.0*rn-1.0)*chi1/x-chi0
      xi=cmplx(apsi,-chi)
      an=(d(n)/refrel+rn/x)*apsi-apsi1
      an=an/((d(n)/refrel+rn/x)*xi-xi1)

      bn=(refrel*d(n)+rn/x)*apsi-apsi1
      bn=bn/((refrel*d(n)+rn/x)*xi-xi1)

      qsca=qsca+(2.0*rn+1.0)*(cabs(an)*cabs(an)+cabs(bn)*cabs(bn))

      do 789 j=1,nang
         jj=2*nang-j
         pi(j)=pi1(j)
         tau(j)=rn*amu(j)*pi(j)-(rn+1.0)*pi0(j)
         p=(-1.0)**(n-1)
```

```
        s1(j)=s1(j)+fn*(an*pi(j)+bn*tau(j))
        t=(-1.0)**n
        s2(j)=s2(j)+fn*(an*tau(j)+bn*pi(j))
        if (j.eq.jj) goto 789
        s1(jj)=s1(jj)+fn*(an*pi(j)*p+bn*tau(j)*t)
        s2(jj)=s2(jj)+fn*(an*tau(j)*t+bn*pi(j)*p)
 789  continue

      psi0=psi1
      psi1=psi
      apsi1=psi1
      chi0=chi1
      chi1=chi
      xi1=cmplx(apsi1,-chi1)
      n=n+1
      rn=n

      do 999 j=1,nang
         pi1(j)=((2.0*rn-1.0)/(rn-1.0))*amu(j)*pi(j)
         pi1(j)=pi1(j)-rn*pi0(j)/(rn-1.0)
         pi0(j)=pi(j)
 999  continue

      if (n-1-nstop) 200, 300, 300

 300  continue
      qsca=(2.0/(x*x))*qsca
      qext=(4.0/(x*x))*float(s1(1))
      qback=(4.0/(x*x))*cabs(s1(2*nang-1))*cabs(s1(2*nang-1))

      end

      FUNCTION rtbis(func,x1,x2,xacc)
      INTEGER JMAX
      REAL rtbis,x1,x2,xacc,func
      EXTERNAL func
      PARAMETER (JMAX=80)
      INTEGER j
      REAL dx,f,fmid,xmid
      fmid=func(x2)
      f=func(x1)

C     if(f*fmid.ge.0.) pause 'root must be bracketed in rtbis'
      if(f*fmid.ge.0.) then
         rtbis=-101.0
         return
      endif

      if(f.lt.0.)then
        rtbis=x1
        dx=x2-x1
      else
        rtbis=x2
        dx=x1-x2
      endif
      do 11 j=1,JMAX
        dx=dx*.5
        xmid=rtbis+dx
        fmid=func(xmid)
        if(fmid.le.0.)rtbis=xmid
```

```
      if(abs(dx).lt.xacc .or. fmid.eq.0.) return
11    continue

C     pause 'too many bisections in rtbis'
      rtbis=-102.0

      END
C  (C) Copr. 1986-92 Numerical Recipes Software 41]3Y2r1..
```

Appendix 2

Calculation of r from Eq. [59] for a prolate spheroid

i.e. solution of the equation

$$\left(\frac{d_{sps}}{d_{lsps}}\right)\sqrt{\frac{s_{ps}}{s_{sp}}} = \frac{\sqrt{\dfrac{\ln(r+\sqrt{(r^2-1)})}{r\sqrt{(r^2-1)}}}}{\sqrt{\dfrac{1}{2r}}\sqrt{\dfrac{1}{r}+\dfrac{r\arctan\sqrt{(r^2-1)}}{\sqrt{r^2-1}}}}$$

```
$declare
c
c     Arguments:
c     ds    : Stokes diameter
c     dls   : light scattering diameter
c     rpr   : real part of particle refractive index
c     rpi   : imag. part of particle ref. index
c     rm    : real part of medium ref. index
c     wl    : wavelength of laser light
c     *****************************************
c     wl, ds and dls must have the same units (i.e. um)
c     *****************************************

          double precision function lom(a_ds [value], a_dls [value],
          +    a_rpr [value], a_rpi [value], a_rm [value], a_wl [value])


      complex s1(20),s2(20),refrel
      real ds,dls,rpr,rpi,rm,wl
      real x,qext,qsca,qback, sps, ssp, sspold, dssp
      real rmax, rmin, r, dv, a
      integer iter
      real zero, rtbis
      external zero

      real tmp

      common /arg/ ds, dls, sps, ssp

      real C_PI, C_TOL
      integer C_MAXITER, C_NANG
      parameter(C_PI=3.1415926536,
     +         C_TOL=1.0e-4,
     +        C_MAXITER=100,
     +        C_NANG=3)

C     ******************************

      ds=a_ds
      dls=a_dls
      rpr=a_rpr
      rpi=a_rpi
      rm=a_rm
      wl=a_wl
```

```
      refrel=cmplx(rpr,rpi)/rm

      x=C_PI*dls*rm/wl
      call bhmie(x,refrel,C_NANG,s1,s2,qext,qsca,qback)
      sps=qsca
c     ****************************************
c     Start iteration for finding r
c     ****************************************
      ssp=sps
      iter=0
 10   continue

        sspold=ssp
        rmax=10.0
        rmin=1.0+epsilon(rmin)

 20     continue

        r=rtbis(zero,rmin,rmax,C_TOL)
c       ****************************************
c       If the root is not in the interval [rmin,rmax], increase rmax.
c       Note ! the upper limit is related to the maximum  number
        of iterations in rtbis.
c       ****************************************
        if ((r.eq.-101.0).and.(rmax.le.1.0e16)) then
           rmax=rmax*10.0
           goto 20
        endif
c       ****************************************
c       Make sure that rtbis did not fail.
c       ****************************************
        if (r.lt.0.0) then
           lom=r
           goto 999
        endif

        a=ds/sqrt( (1.0/(r*sqrt(r**2-1.0))) * log(r+sqrt(r**2-1.0)) )
        dv=a/(r**(2.0/3.0))

        x=C_PI*dv*rm/wl
        call bhmie(x,refrel,C_NANG,s1,s2,qext,qsca,qback)
        ssp=qsca

        iter=iter+1
        if (iter.gt.C_MAXITER) then
           lom=-1.0
           goto 999
        endif
c       ****************************************
c       rfunc(r) is bounded by ] 0, 1 [
c       ****************************************
        tmp=ds/dls*sqrt(sps/ssp)
        if (ds/dls*sqrt(sps/ssp).gt.1.0) then
           lom=-2.0
           goto 999
        endif

        dssp=abs((ssp-sspold)/ssp)
        if (dssp.le.C_TOL) then
```

```
            lom=r
            goto 999
          endif

      goto 10

 999  continue
c      write(6,*) 'Iter = ', iter
c      write(6,*) 'Zero =' , zero(r)
c      write(6,*) 'rmax =' , rmax
      end

C**********************************************************************
      real function rfunc(r)
      real r
      real f0,f1,f2

      f0=sqrt(1.0/(r*sqrt(r**2-1.0))* log(r+sqrt(r**2-1.0)))
      f1=1.0/sqrt(2.0*r)
      f2=sqrt(1.0/r + r/(sqrt(r**2-1))*atan(sqrt(r**2-1.0)))

      rfunc=f0/(f1*f2)

      end
C**********************************************************************
      real function zero(r)
      real r, ds, dls, sps, ssp
      common /arg/ ds, dls, sps, ssp
      real rfunc
      real f1,f2,f3

      f1=rfunc(r)
      f2=(ds/dls)*sqrt(sps/ssp)
      f3=f1-f2
      zero=f3

      end
C**********************************************************************

      subroutine bhmie(x, refrel, nang, s1, s2, qext, qsca, qback)

      complex s1(20), s2(20)
      real x, qext, qsca, qback
      integer nang

      real amu(10), theta(10), pi(10), tau(10), pi0(10), pi1(10)
      complex d(3000), y, refrel, xi, xi0, xi1, an, bn
      double precision psi0, psi1, psi, dn, dx

      real xstop, ymod, dang, rn, chi0, chi1, apsi0, apsi1
      real fn, chi, apsi, p, t
      integer nstop, nmx, j, nn, n, jj

      real C_PI
      parameter(C_PI=3.1415926536)

C     ******************************

      dx=x
      y=x*refrel
```

```
      xstop=x+4.0*x**(1.0/3.0)+2.0
      nstop=xstop
      ymod=cabs(y)
      nmx=amax1(xstop,ymod)+15
      dang=C_PI/2.0/float(nang-1)

      do 555 j=1,nang
         theta(j)=(float(j)-1.0)*dang
         amu(j)=cos(theta(j))
  555 continue

      d(nmx)=cmplx(0.0,0.0)
      nn=nmx-1
      do 120 n=1,nn
         rn=nmx-n+1
         d(nmx-n)=(rn/y)-(1.0/(d(nmx-n+1)+rn/y))
  120 continue

      do 666 j=1,nang
         pi0(j)=0.0
         pi1(j)=1.0
  666 continue

      nn=2*nang-1
      do 777 j=1,nn
         s1(j)=cmplx(0.0,0.0)
         s2(j)=cmplx(0.0,0.0)
  777 continue

      psi0=dcos(dx)
      psi1=dsin(dx)
      chi0=-sin(x)
      chi1=cos(x)
      apsi0=psi0
      apsi1=psi1
      xi0=cmplx(apsi0,-chi0)
      xi1=cmplx(apsi1,-chi1)
      qsca=0.0
      n=1

  200 dn=n
      rn=n
      fn=(2.0*rn+1.0)/(rn*(rn+1.0))
      psi=(2.0*dn-1.0)*psi1/dx-psi0
      apsi=psi
      chi=(2.0*rn-1.0)*chi1/x-chi0
      xi=cmplx(apsi,-chi)
      an=(d(n)/refrel+rn/x)*apsi-apsi1
      an=an/((d(n)/refrel+rn/x)*xi-xi1)

      bn=(refrel*d(n)+rn/x)*apsi-apsi1
      bn=bn/((refrel*d(n)+rn/x)*xi-xi1)

      qsca=qsca+(2.0*rn+1.0)*(cabs(an)*cabs(an)+cabs(bn)*cabs(bn))

      do 789 j=1,nang
         jj=2*nang-j
         pi(j)=pi1(j)
         tau(j)=rn*amu(j)*pi(j)-(rn+1.0)*pi0(j)
```

```
        p=(-1.0)**(n-1)
        s1(j)=s1(j)+fn*(an*pi(j)+bn*tau(j))
        t=(-1.0)**n
        s2(j)=s2(j)+fn*(an*tau(j)+bn*pi(j))
        if (j.eq.jj) goto 789
        s1(jj)=s1(jj)+fn*(an*pi(j)*p+bn*tau(j)*t)
        s2(jj)=s2(jj)+fn*(an*tau(j)*t+bn*pi(j)*p)
 789  continue

      psi0=psi1
      psi1=psi
      apsi1=psi1
      chi0=chi1
      chi1=chi
      xi1=cmplx(apsi1,-chi1)
      n=n+1
      rn=n

      do 999 j=1,nang
         pi1(j)=((2.0*rn-1.0)/(rn-1.0))*amu(j)*pi(j)
         pi1(j)=pi1(j)-rn*pi0(j)/(rn-1.0)
         pi0(j)=pi(j)
 999  continue

      if (n-1-nstop) 200, 300, 300

 300  continue
      qsca=(2.0/(x*x))*qsca
      qext=(4.0/(x*x))*real(s1(1))
      qback=(4.0/(x*x))*cabs(s1(2*nang-1))*cabs(s1(2*nang-1))

      end

     FUNCTION rtbis(func,x1,x2,xacc)
      INTEGER JMAX
      REAL rtbis,x1,x2,xacc,func
      EXTERNAL func
      PARAMETER (JMAX=80)
      INTEGER j
      REAL dx,f,fmid,xmid
      fmid=func(x2)
      f=func(x1)

C     if(f*fmid.ge.0.) pause 'root must be bracketed in rtbis'
      if(f*fmid.ge.0.) then
         rtbis=-101.0
         return
      endif

      if(f.lt.0.)then
        rtbis=x1
        dx=x2-x1
      else
        rtbis=x2
        dx=x1-x2
      endif
      do 11 j=1,JMAX
        dx=dx*.5
        xmid=rtbis+dx
        fmid=func(xmid)
```

```
      if(fmid.le.0.)rtbis=xmid
      if(abs(dx).lt.xacc .or. fmid.eq.0.) return
11    continue

C     pause 'too many bisections in rtbis'
      rtbis=-102.0

      END

C  (C) Copr. 1986-92 Numerical Recipes Software 41]3Y2r1..
```